

REPORT DOCUMENTATION PAGE		READ INSTRUCTIONS BEFORE COMPLETING FORM
1. REPORT NUMBER TR 7221	2. GOVT ACCESSION NO.	3. RECIPIENT'S CATALOG NUMBER
4. TITLE (and Subtitle) IMPLEMENTATION OF THE LAMONT-DOHERTY GEOLOGICAL OBSERVATORY NORMAL MODE/FAST FIELD MODEL ON THE NUSC VAX 780/11 COMPUTER		5. TYPE OF REPORT & PERIOD COVERED
		6. PERFORMING ORG. REPORT NUMBER
7. AUTHOR(s) D. J. Thomson (Exchange Scientist from Defence Research Establishment Pacific, Victoria, B.C. Canada)		8. CONTRACT OR GRANT NUMBER(s)
9. PERFORMING ORGANIZATION NAME AND ADDRESS Naval Underwater Systems Center New London Laboratory New London, CT 06320		10. PROGRAM ELEMENT, PROJECT, TASK AREA & WORK UNIT NUMBERS 633K17
11. CONTROLLING OFFICE NAME AND ADDRESS Naval Underwater Systems Center New London Laboratory New London, CT 06320		12. REPORT DATE 18 September 1984
		13. NUMBER OF PAGES 52
14. MONITORING AGENCY NAME & ADDRESS (if different from Controlling Office)		15. SECURITY CLASS. (of this report) UNCLASSIFIED
		15a. DECLASSIFICATION/DOWNGRADING SCHEDULE
16. DISTRIBUTION STATEMENT (of this Report)  Approved for public release; distribution unlimited.		
17. DISTRIBUTION STATEMENT (of the abstract entered in Block 20, if different from Report)		
18. SUPPLEMENTARY NOTES		
19. KEY WORDS (Continue on reverse side if necessary and identify by block number) Branch Line Integral      Fast Field Model      Sound Propagation Continuous Spectrum      Fast Fourier Transform Contour Integral      Green's Function Discrete Spectrum      Liquid/Solid Layers Excitation Function      Normal Mode Model		
20. ABSTRACT (Continue on reverse side if necessary and identify by block number)  A computer model that evaluates the integral solution representing the acoustic field due to a harmonic point source in a layered fluid/solid medium has been implemented on the NUSC VAX 780/11 computer. The model was developed by Dr. H. W. Kutschale of the Lamont-Doherty Geological Observatory. The version obtained by NUSC, designated 17HH, permits two computation methods. They are (1) a normal mode method, which evaluates the field as a finite sum of propagating modes (discrete spectrum) plus a branch line integral (continuous		

20. (Continued)

spectrum), and (2) a fast field method, which effects a direct numerical evaluation of the integral solution via a fast Fourier transform. This report provides NUSC users with sufficient documentation for running the model to obtain predictions of sound propagation. Several test casts are presented, which illustrate various features and capabilities of the model.

NUSC Technical Report 7221  
18 September 1984

LIBRARY  
RESEARCH REPORTS DIVISION  
NAVAL POSTGRADUATE SCHOOL  
MONTEREY, CALIFORNIA 93943

# **Implementation of the Lamont-Doherty Geological Observatory Normal Mode/Fast Field Model on the NUSC VAX 780/11 Computer**

D. J. Thomson  
Surface Ship Sonar Department



**Naval Underwater Systems Center**  
**Newport, Rhode Island / New London, Connecticut**

## **PREFACE**

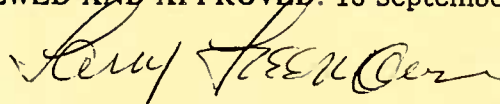
This report was prepared under Project No. 633K17. The sponsoring activity was the Surface Ship Sonar Department (Code 33), Naval Underwater Systems Center. The research for this work was funded principally by the Defence Research Establishment Pacific, Victoria, British Columbia, Canada.

The version of the computer model described herein was provided by Dr. W. A. Kuperman, Head of the Numerical Modelling Division at the Naval Ocean Research and Development Agency, NSTL Station, Mississippi.

It is a pleasure to acknowledge the helpful discussions with Dr. H. W. Kutschale of the Lamont-Doherty Geological Observatory in Palisades, New York, concerning the implementation and modification of the computer code.

The Technical Reviewer for this document was Roy Deavenport (Code 3331).

**REVIEWED AND APPROVED: 18 September 1984**

A handwritten signature in dark ink, appearing to read 'Larry Freeman', is written over the printed name.

**LARRY FREEMAN**  
**Head, Surface Ship Sonar Department**

Dr. D. J. Thomson is an exchange scientist from the Defence Research Establishment Pacific, FMO, Victoria, British Columbia, V0S 1B0, Canada. He is presently located at the New London Laboratory, Naval Underwater Systems Center, New London, Connecticut 06320.

## TABLE OF CONTENTS

	Page
LIST OF ILLUSTRATIONS .....	iii
1. INTRODUCTION .....	1
2. BASIC THEORY .....	2
2.1 Mathematical Model .....	2
2.2 Basic Equations .....	2
2.3 Normal Mode Representation .....	6
2.4 Fast Field Representation .....	7
2.5 Discussion .....	8
3. DATA INPUT SEQUENCES .....	11
3.1 Data Sequence for NUSC17HH .....	11
3.2 Data Sequence for PLØT17HH .....	16
4. COMMAND FILE SEQUENCE .....	17
5. NUMERICAL EXAMPLES .....	18
5.1 Test Case 1 .....	18
5.2 Test Case 2 .....	27
5.3 Test Case 3 .....	33
5.4 Test Case 4 .....	39
6. SUMMARY .....	44
7. REFERENCES .....	45
APPENDIX -- EQUIVALENCE BETWEEN LDGO AND NUSC DATA INPUT SEQUENCES .....	47

## LIST OF ILLUSTRATIONS

Figure		Page
1	The Layered Model Showing (a) Layer Index Notation, and (b) Variation of Acoustic Properties within $z_j < z < z_{j+1}$ .....	3
2	Sketch of the Complex Wavenumber Plane Showing the Location of the Discrete Mode Eigenvalues (poles), the Branch Cut (xxxxx), and the Contour (.....) for the Branch Line Integral .....	6
3	Basic Computational Options for NUSC17HH .....	10
4	Data Input Sequence for Test Case 1 .....	19
5	Sound Speed Profile for Test Case 1 (Source Depth = 253.9 m, Receiver Depth = 863.5 m, $c_{N+1} = 1555.52$ m/s, $\rho_{N+1} = 1.9176$ g/cm <sup>3</sup> )	20
6	(a) Mode Excitation Functions Versus Wavenumber, and (b) Associated Propagation Losses Versus Range Test Case 1, Discrete Spectrum, Frequency = 25 Hz .....	21
7	(a) Green's Function Kernel Versus Wavenumber, and (b) Associated Propagation Losses Versus Range Test Case 1, Discrete Spectrum, Frequency = 25 Hz .....	22
8	Fast Field Propagation Losses Versus Range, Test Case 1 Discrete Plus Continuous Spectrum, Frequency = 25 Hz (a) NØFFT = 512, CMAX = 1555.52 m/s, Source Aperture < 11.6° (b) NØFFT = 1024, CMAX = 1649.43 m/s, Source Aperture < 22.5° ....	24
9	Fast Field Propagation Losses Versus Range, Test Case 1 Discrete Plus Continuous Spectrum, Frequency = 25 Hz (a) NØFFT = 2048, CMAX = 1875.95 m/s, Source Aperture < 35.7° (b) NØFFT = 4096, CMAX = 2586.31 m/s, Source Aperture < 53.9° ....	25
10	(a) Mode Excitation Functions Versus Wavenumber, and (b) Associated Propagation Losses Versus Range Test Case 1, Discrete Spectrum, Frequency = 250 Hz .....	26
11	Data Input Sequence for Test Case 2 .....	28
12	Sound Speed Profile for Test Case 2 (Source Depth = 91.44 m, Receiver Depth = 137.14 m, $c_{N+1} = 1507.14$ m/s, $\rho_{N+1} = 1.0$ g/cm <sup>3</sup> )	29
13	(a) Green's Function Kernel Versus Wavenumber, and (b) Associated Propagation Losses Versus Range Test Case 2, Discrete Spectrum, Frequency = 50 Hz, $\sigma = 0$ m .....	30
14	(a) Green's Function Kernel Versus Wavenumber, and (b) Associated Propagation Losses Versus Range Test Case 2, Discrete Spectrum, Frequency = 50 Hz, $\sigma = 5$ m .....	31

## LIST OF ILLUSTRATIONS (Cont'd)

Figure		Page
15	(a) Green's Function Kernel Versus Wavenumber, and (b) Associated Propagation Losses Versus Range Test Case 2, Discrete Spectrum, Frequency = 50 Hz, 5 m Ice Canopy	32
16	Data Input Sequence for Test Case 3 .....	34
17	Sound Speed Profile for Test Case 3 (Source Depth = 30 m, Receiver Depth = 90 m, $c_{N+1} = 1505$ m/s, $\rho_{N+1} = 2.1$ g/cm <sup>3</sup> ) .....	35
18	(a) Mode Excitation Functions Versus Wavenumber, and (b) Associated Propagation Losses Versus Range Test Case 3, Discrete Spectrum, Frequency = 100 HZ .....	36
19	(a) Green's Function Kernel Versus Wavenumber, and (b) Associated Propagation Losses Versus Range Test Case 3, NØFFT = 1024, CMAX = 1650 m/s, Frequency = 100 Hz ...	37
20	Propagation Losses Versus Range, Test Case 3, Frequency = 100 Hz (a) Fast Field Method, NØFFT = 2048, CMAX = 1650 m/s (b) Normal Mode Method, NØFFT = 4096, ICØNT < 0 .....	38
21	Data Input Sequence for Test Case 4 .....	40
22	Sound Speed Profile for Test Case 4 ( $c_{N+1} = 1590$ m/s, $\rho_{N+1} = 1.2$ g/cm <sup>3</sup> , $\alpha_{N+1} = 76.83$ dB/km) .....	41
23	(a) Green's Function Kernel Versus Wavenumber, and (b) Associated Propagation Losses Versus Range, Test Case 4 Source Depth = Receiver Depth = 50.0 m, Frequency = 250 Hz .....	42
24	(a) Green's Function Kernel Versus Wavenumber, and (b) Associated Propagation Losses Versus Range, Test Case 4 Source Depth = Receiver Depth = 99.5 m, Frequency = 250 Hz .....	43



IMPLEMENTATION OF THE  
LAMONT-DOHERTY GEOLOGICAL OBSERVATORY NORMAL MODE/FAST FIELD MODEL  
ON THE NUSC VAX 780/11 COMPUTER

## 1. INTRODUCTION

A common boundary value problem in underwater acoustics is to determine the sound pressure field caused by a harmonic point source located within a plane multilayered medium. The classic solution to this problem, when cast in a cylindrical coordinate system, takes the form of a Hankel transform.<sup>1</sup> This integral solution can be manipulated to produce several different representations for the field<sup>2</sup> from which numerical evaluations can be obtained.<sup>3</sup> A recent survey<sup>4,5</sup> lists existing computer models based on these representations and aimed at obtaining predictions of sound propagation for use in sonar applications.

Most of the models in the above survey deal with the propagation of pressure waves within layered liquid media. An exception is found in the models developed by Kutschale, which account for both pressure-wave and shear-wave propagation within layered liquid/solid media.<sup>6,7</sup> Kutschale's models were originally developed for application in the Arctic Ocean, where the combination of a solid ice canopy and an upward refracting ocean sound speed profile requires the capability for modeling the interaction between the two types of waves. More recently, for shallow water environments, there has been interest in modeling the loss of acoustic energy into the ocean bottom as a result of pressure-wave to shear-wave conversion.<sup>8</sup> Of course, geophysicists have always been concerned with the propagation of seismic waves in layered solid media.<sup>9,10</sup>

This report describes the implementation of Kutschale's LDGO normal mode/fast field model on the NUSC VAX 780/11 computer. The version obtained by NUSC, designated 17HH, permits two computational methods for evaluating the field due to a point source located within a layered fluid/solid medium: (1) a normal mode method, in which the field is represented as a finite sum of propagating modes (discrete spectrum) plus a branch line integral (continuous spectrum), and (2) a fast field method, in which the field is represented in the form of a finite Fourier integral whose evaluation can proceed directly via a fast Fourier transform (FFT). In addition to the capability for treating propagation of both compressional and shear waves, the 17HH model can accommodate the effects of rough boundaries via new boundary conditions derived from perturbation analysis.<sup>11,12</sup> We designate the NUSC version of the computer code as NUSC17HH.

Section 2 summarizes the basic theory leading to the two representations of the field used by NUSC17HH and presents some of the computational limitations of the normal mode option that must be considered when running the model. Section 3 presents a detailed description of the data input sequence required to obtain NUSC17HH predictions of sound propagation and the data input sequence that must be supplied to a locally developed plotting program (PLØT17HH). Section 4 describes a sample command file structure needed to run the model as a batch job submission. Finally, in Section 5 we present several numerical examples that illustrate various features and capabilities of the model.



## 2. BASIC THEORY

### 2.1 MATHEMATICAL MODEL

Let the half-space  $z > 0$  ( $z$  positive down) of a cylindrical coordinate system  $(r, \theta, z)$  be occupied by a layered elastic medium as shown in figure 1. Each layer is characterized by five material properties, i.e., compressional wave sound speed ( $c$ ), shear wave sound speed ( $v$ ), compressional wave attenuation ( $\alpha$ ), shear wave attenuation ( $\beta$ ), and density ( $\rho$ ). The parameters  $v_j$ ,  $\alpha_j$ ,  $\beta_j$ , and  $\rho_j$  are presumed to be constant within the  $j^{\text{th}}$  layer. The compressional sound speed,  $c_j$ , is presumed to vary with depth according to  $1/c_j^2(z) = a_j + b_j z$ . The layer constants  $a_j$  and  $b_j$  are determined by the values of  $c_j$  at  $z_j+0$  and  $z_{j+1}-0$ . The region  $z > z_N$  is taken to be a homogeneous solid (or liquid) whereas the region  $z < 0$  is taken to be a homogeneous fluid (or vacuum). In this model, layer interfaces are presumed to occur at both the source and receiver depths. Any discontinuities in material properties of the medium can be accommodated at a layer interface.

### 2.2 BASIC EQUATIONS

With the passage of a harmonic ( $e^{-i\omega t}$ ,  $\omega = 2\pi f$ ) elastic wave through the  $j^{\text{th}}$  layer, the resulting particle displacement within  $z_j < z < z_{j+1}$  can be found by solving the reduced wave equations satisfied by the two displacement potentials,  $\phi_j$  and  $\psi_j$ ,<sup>9</sup> i.e.,

$$\nabla^2 \phi_j + \frac{\omega^2}{c_j^2} \phi_j = 0, \quad (1)$$

and

$$\nabla^2 \psi_j + \frac{\omega^2}{v_j^2} \psi_j = 0, \quad (2)$$

where

$$\nabla^2 = \frac{1}{r} \frac{\partial}{\partial r} \left( r \frac{\partial}{\partial r} \right) + \frac{\partial^2}{\partial z^2}. \quad (3)$$

The vertical ( $q_j$ ) and horizontal ( $w_j$ ) components of displacement are recovered from these potentials by differentiation, i.e.,

$$q_j = \frac{\partial \phi_j}{\partial r} + \frac{\partial^2 \psi_j}{\partial r \partial z}, \quad (4)$$

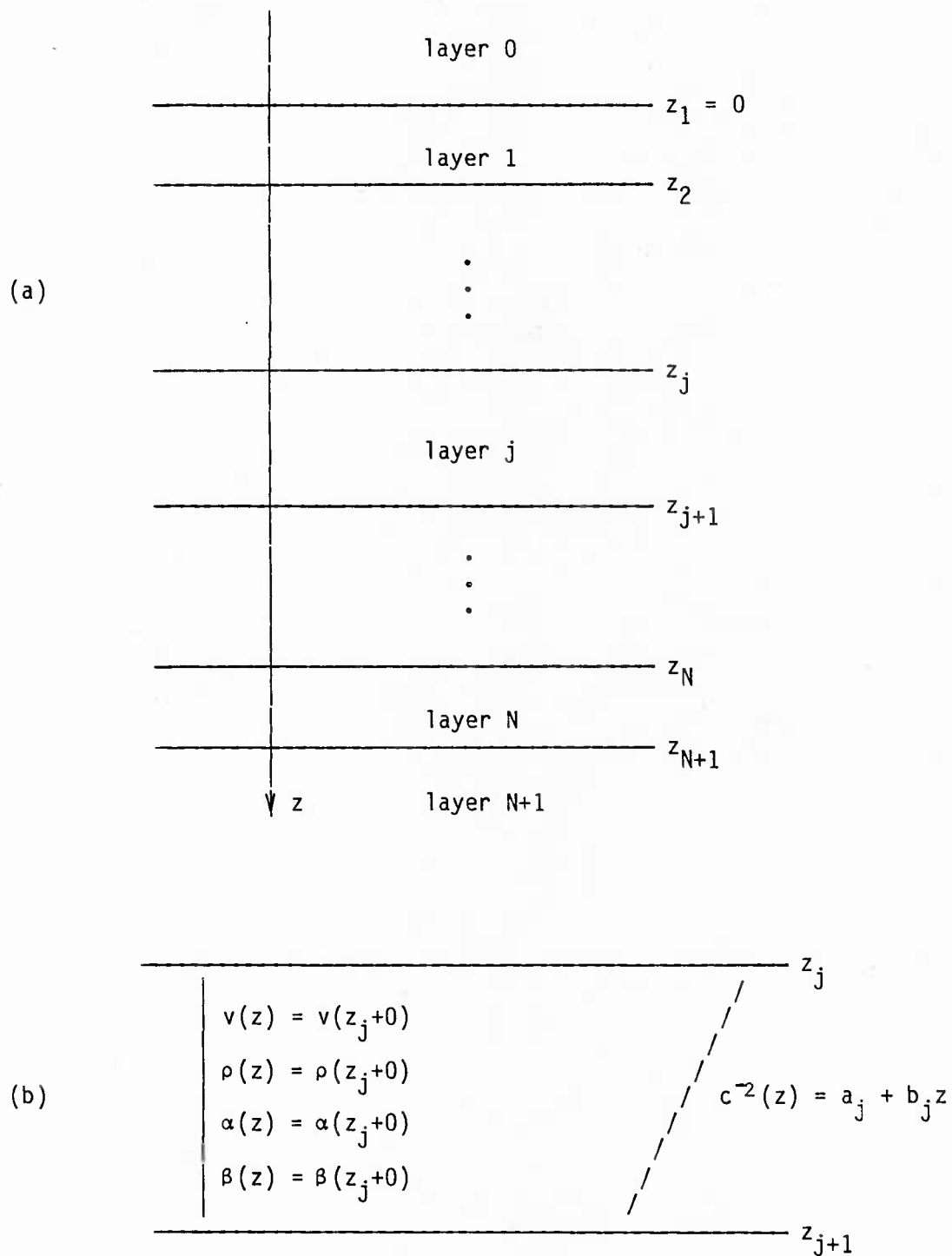


Figure 1. The Layered Model Showing (a) Layer Index Notation, and (b) Variation of Acoustic Properties within  $z_j < z < z_{j+1}$

and

$$w_j = \frac{\partial \phi_j}{\partial z} + \frac{\partial^2 \psi_j}{\partial z^2} + \frac{\omega^2}{v_j^2} \psi_j . \quad (5)$$

Similarly, the normal ( $p_{zz}$ ) and tangential ( $p_{rz}$ ) components of stress are obtained via

$$p_{zz} = \lambda_j \frac{\omega^2}{c_j^2} \phi_j + 2\mu_j \frac{\partial w_j}{\partial z} , \quad (6)$$

and

$$p_{rz} = \mu_j \left( \frac{\partial q_j}{\partial z} + \frac{\partial w_j}{\partial r} \right) . \quad (7)$$

Here  $\lambda_j$  and  $\mu_j$  are Lamé's elastic parameters which are related to the sound speeds and density by

$$\rho_j c_j^2 = \lambda_j + 2\mu_j , \quad (8)$$

and

$$\rho_j v_j^2 = \mu_j . \quad (9)$$

Equations (1) and (2) are conveniently solved using Hankel transforms. The displacement potentials  $\phi_j$  and  $\psi_j$  can be represented in the form

$$\phi_j(r, z) = \int_0^\infty f_j(k, z) J_0(kr) k dk , \quad (10)$$

and

$$\psi_j(r, z) = \int_0^\infty g_j(k, z) J_0(kr) k dk , \quad (11)$$

where  $J_0$  is the Bessel function of the first kind,  $k$  is the horizontal wavenumber, and  $f_j$  and  $g_j$  are solutions to the depth-dependent equations

$$\frac{d^2 f_j}{dz^2} + \left( \frac{\omega^2}{c_j^2} - k^2 \right) f_j = 0 , \quad (12)$$

and

$$\frac{d^2 g_j}{dz^2} + \left( \frac{\omega^2}{v_j^2} - k^2 \right) g_j = 0 . \quad (13)$$

If  $c_j$  and  $v_j$  are constant within a layer, then both  $f_j$  and  $g_j$  are linear combinations of complex exponential functions representing upgoing and downgoing waves. When  $1/c_j^2$  is a linear function of  $z$ , then the appropriate solution to equation (12) comprises a linear combination of Airy functions.<sup>1,3,15</sup> Each  $f_j$  and  $g_j$  involves two arbitrary constants that must be determined for each layer. For  $j = 0$  and  $j = N+1$ , the potentials  $\phi_j$  and  $\psi_j$  must tend to zero as  $|z| \rightarrow \infty$ . The remaining conditions for determining the constants are provided by requiring the solutions to equations (12) and (13) in each layer to satisfy appropriate boundary conditions at layer interfaces. For elastic media in "welded contact," the components of displacement,  $q_j$  and  $w_j$ , and stress,  $(p_{zz})_j$  and  $(p_{rz})_j$ , remain continuous across the planes  $z = z_j$  and  $z = z_{j+1}$ . These continuity requirements are sufficient to determine the unique solutions to the depth-dependent equations for layered media. Although equations (1), (2), (12), and (13) hold only in source-free regions, the inclusion of a point acoustic source can be accommodated by requiring that the displacement potentials  $\phi_j$  and  $\psi_j$  satisfy additional boundary conditions on the plane  $z = z_s$ .<sup>9</sup>

For  $z > z_s$ , each displacement potential for the layered medium can be cast in the canonical form<sup>16,17</sup>

$$\phi(r, z) = \int_0^\infty \frac{A(k)}{\Delta(k)} U(z_s, k) V(z, k) J_0(kr) k dk , \quad (14)$$

and

$$\psi(r, z) = \int_0^\infty \frac{B(k)}{\Delta(k)} U(z_s, k) V(z, k) J_0(kr) k dk , \quad (15)$$

where the multipliers of  $J_0(kr)kdk$  represent the Green's function solutions to the systems of depth-dependent equations and can be determined from the layer solutions  $f_j$  and  $g_j$ ,  $j = 0, 1, \dots, N+1$  using the classic Thomson-Haskell

matrix approach.<sup>5,6,15</sup> Here  $U(z,k)$  represents the solution to equation (12) that satisfies all boundary conditions for  $z < z_s$ , and  $V(z,k)$  represents the solution that satisfies all boundary conditions for  $z > z_s$ . When  $z < z_s$ , the appropriate form of each potential is obtained by interchanging  $z$  and  $z_s$  in equations (14) and (15). The denominator  $\Delta(k) = \rho(z_s)W(k)$  where  $W(k)$  is the Wronskian of  $U$  and  $V$ , i.e.,  $W(k) = V(z_s,k)U_z(z_s,k) - V_z(z_s,k)U(z_s,k)$ . These Green's functions account for all the environmental properties of the layered medium, as well as the locations of the source and receiver. Their evaluation for any problem constitutes the major computational effort required to obtain predictions of sound propagation.

### 2.3 NORMAL MODE REPRESENTATION

Integrals of the form in equations (14) and (15) are improper. For lossless media, the Green's functions appearing in the integrands are singular at (real) roots of  $\Delta(k)$ . Using the contour integral techniques presented by Ewing, Jardetzky and Press,<sup>9</sup> the modal representation for the displacement potential  $\phi$  is given by

$$\begin{aligned} \phi(r,z) = & \sum_{m=1}^M C_0(k_m) U(z_s, k_m) U(z, k_m) H_0^{(1)}(k_m r) \\ & + \int_{BL} C_1(k) U(z_s, k) U(z, k) H_0^{(1)}(kr) k dk, \end{aligned} \quad (16)$$

with a similar representation for  $\psi$ . The discrete wavenumbers  $k_m$ ,  $m = 1, \dots, M$  are roots of the period equation,  $\Delta(k)=0$ . For lossless liquid media, the

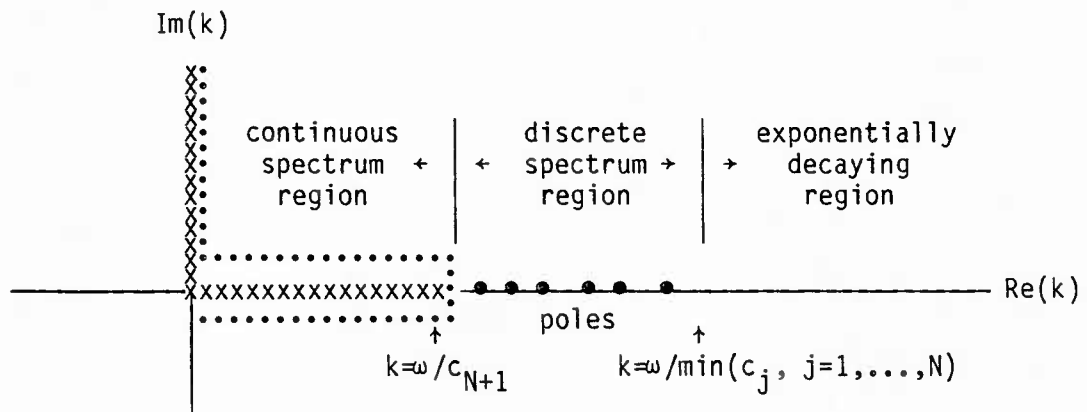


Figure 2. Sketch of the Complex Wavenumber Plane Showing the Location of the Discrete Mode Eigenvalues (poles), the Branch Cut (xxxxx) and the Contour (.....) for the Branch Line Integral

location of these poles and the branch line contour (BL) is depicted in figure 2. For elastic media, two branch line contours are obtained, associated with the branch points at  $k=\omega/c_{N+1}$  and  $k=\omega/v_{N+1}$ . Each term appearing in the sum is termed a normal mode. The factor  $U(z_s, k_m)$  determines the influence of the source on each mode amplitude. The vertical distribution of each mode is described by the factor  $U(z, k_m)$ . The coefficient  $C_0$  gives the relative excitation of each mode. In the case of liquid layers for which  $1/c_j^2$  varies linearly with depth  $z$ , explicit expressions for the coefficients  $C_0$  and  $C_1$  may be found in Stickler's paper.<sup>15</sup>

#### 2.4 FAST FIELD REPRESENTATION

Although equations (14) and (15) are improper, the significant contribution to these integrals occurs within a finite range of the wavenumber axis,  $k_0 < k < k_{\max}$ . This suggests that these integrals may be evaluated by numerical quadrature. An efficient method for carrying out the numerical integrations is possible if the integrals can be manipulated into the form of finite Fourier integrals so that the FFT algorithm can be used. In underwater acoustics applications, this approach is known as the fast field method.<sup>1, 3, 7</sup>

To this end, we use the identity  $2J_0(kr) = H_0^{(1)}(kr) - H_0^{(1)}(-kr)$  to cast equation (14) in the equivalent form

$$\phi(r, z) = \int_{-\infty}^{\infty} D(z, z_s; k) H_0^{(1)}(kr) k dk, \quad (17)$$

where we have set  $D(z, z_s; k) = A(k)[2\Delta(k)]^{-1} U(z_s, k) U(z, k)$ . Next, for  $kr \gg 1$ , we replace the Hankel function  $H_0^{(1)}(kr)$  by the first term in its asymptotic expansion, i.e.,

$$H_0^{(1)}(kr) \sim (2/\pi ikr)^{1/2} \exp(ikr). \quad (18)$$

Under these conditions, the integral appearing in equation (17) may be approximated by

$$\begin{aligned} \phi(r, z) &= (2/\pi i r)^{1/2} \int_{k_0}^{k_{\max}} D(z, z_s; k) \exp(ikr) k^{1/2} dk, \\ &= (2/\pi i r)^{1/2} \sum_{m=0}^{N-1} \int_{k_m}^{k_{m+1}} D(z, z_s; k) \exp(ikr) k^{1/2} dk, \end{aligned} \quad (19)$$

where the discrete wavenumber variable  $k_m = k_0 + m\Delta k$ ,  $m=0, 1, \dots, N-1$  has been introduced spanning the range  $k_{\max} - k_0 = (N-1)\Delta k$ . Provided the sampling interval  $\Delta k$  is sufficiently small, the integrals appearing in equation (19) may be evaluated approximately via the Trapezoid Rule leading to the result

$$\phi(r, z) \approx \Delta k (2/\pi i r)^{1/2} \sum_{m=0}^{N-1} D(z, z_s; k_m) \exp(ik_m r) k_m^{1/2}. \quad (20)$$

If the range interval  $r_{\max} - r_0 = (N-1)\Delta r$  is similarly sampled according to  $r_n = r_0 + n\Delta r$ ,  $n=0, 1, \dots, N-1$  subject to the FFT constraint  $\Delta r \Delta k = 2\pi/N$ , the displacement potential of equation (20) has the following finite complex sequence approximation:

$$\phi(r_n, z) \approx \Delta k (2/\pi i r_n)^{1/2} \exp(ik_0 r_n) \sum_{m=0}^{N-1} E_m \exp(2\pi i m n / N). \quad (21)$$

The above series has the desired form of a discrete Fourier series that can be evaluated rapidly using the FFT algorithm provided that  $N$  is a power of 2. The input sequence  $E_m$  is determined to be

$$E_m = k_m^{1/2} D(z, z_s; k_m) \exp(im\Delta k r_0). \quad (22)$$

The result of letting the complex sequence  $E_m$ ,  $m=0, 1, \dots, N-1$  be input to a complex FFT routine is the complex sequence  $\phi(r_n, z)$  at  $N$  distinct range points  $r_n$ ,  $n=0, 1, \dots, N-1$ . Only the first  $N/2$  values are considered valid due to aliasing. It follows that  $N$  estimates of  $E_m$  and consequently  $D(z, z_s; k_m)$  as a function of the sampled wavenumber  $k_m$  are required. The time consuming portion of the fast field method lies in the generation of this sampled depth-dependent Green's function.

## 2.5 DISCUSSION

The normal mode and fast field computational options for NUSC17HH are summarized in figure 3. The program flow for these choices is directed by the two flags IMODE and ICONT. The value ICONT = 0 limits the normal mode representation to the discrete mode sum only. Although the diagram suggests complete symmetry for the two methods of representing the acoustic field, the normal mode implementation is limited by the following constraints:

1. Only flat boundaries can be treated. The rough boundary conditions developed by Kuperman and Ingenito<sup>11,12</sup> have not been incorporated into the modal representation.



2. Only lossless layers can be treated. This implies that  $\alpha_j$  and  $\beta_j$  must be set to zero for all  $j$ ,  $j=0, \dots, N+1$  in the normal mode method.
3. Only the branch line integral associated with the compressional sound speed  $c_{N+1}$  is included if the flag ICØNT  $\neq 0$  is selected. Moreover, only that portion of the branch line integral along the real axis is computed. The contribution of the branch line integral associated with the shear-wave sound speed of the half-space  $z > z_N$  is not evaluated in the 17HH version of the model. In addition, in the evaluation of the branch line integral, the variation of sound speed within each layer is taken to be constant.
4. If ICØNT  $< 0$ , the sampling interval  $\Delta r$  and maximum range  $N\Delta r/2$  which is automatically determined for the branch line contribution is not usually commensurate with the values of DELR and RMAX selected by the user (see NAMELIST &CARD4 of the next Section). In this case, the sampling interval is determined by the distribution of  $N$  equispaced values of  $k$  around the branch cut on the real axis.

The fast field method of NUSC17HH offers the prospective user the most general option for obtaining numerical predictions of sound propagation within a layered liquid/solid medium. With this choice of computational method, both rough boundaries and absorbing media can be accommodated. In addition, the effects of the continuous spectra associated with both the compressional waves and shear waves can be evaluated.

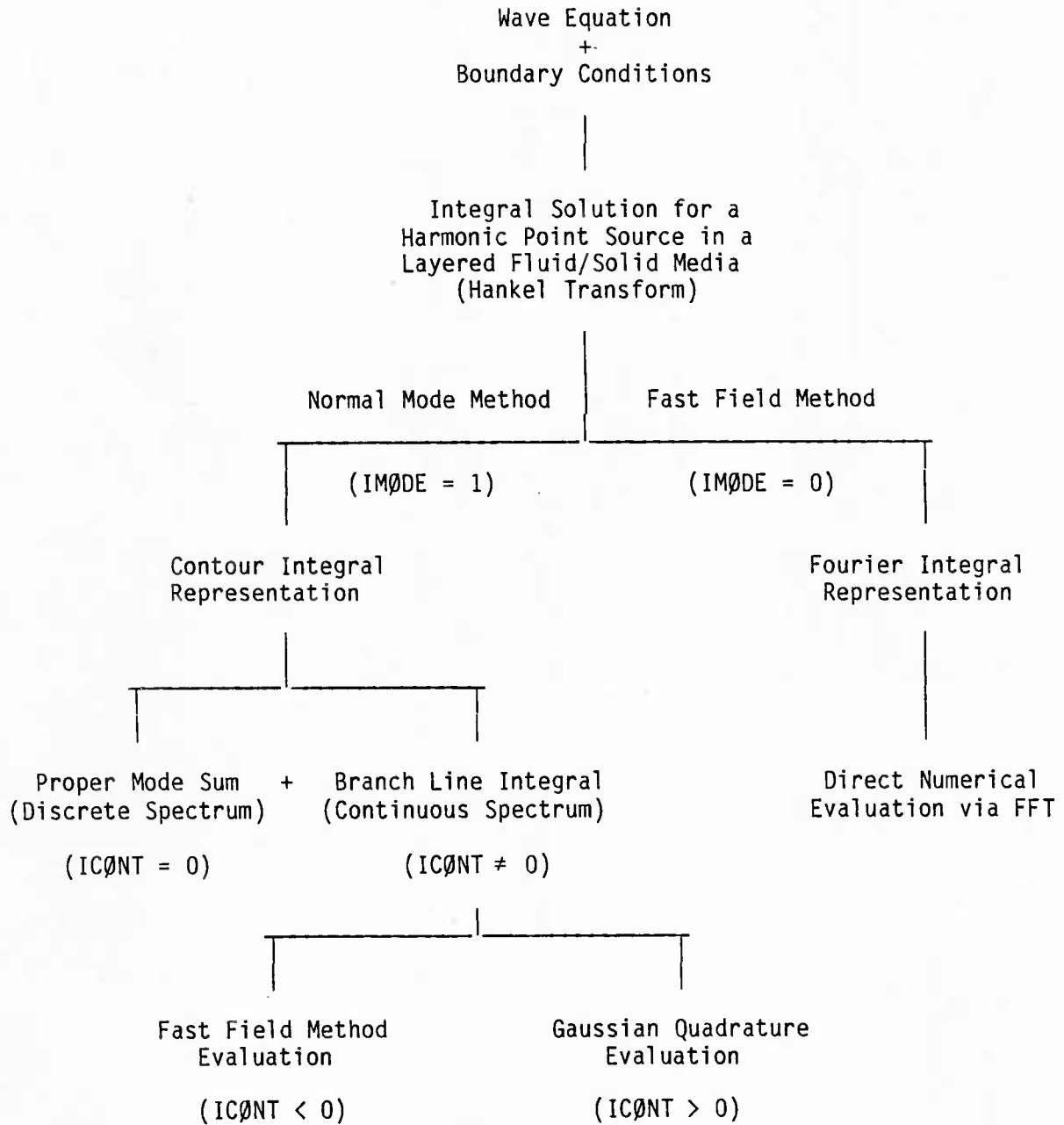


Figure 3. Basic Computational Options for NUSC17HH

## 3. DATA INPUT SEQUENCES

## 3.1 DATA SEQUENCE FOR NUSC17HH

The data input sequence for NUSC17HH has been restructured from that of the LDGO version to make use of the FORTRAN NAMELIST feature. In addition, the input variables have been renamed to make their function more apparent to the casual user. An equivalence list, which relates the NUSC input sequence names to the LDGO sequence names, is provided in the appendix.

CARD 1 -- NAMELIST &CARD1 inputs NØSSP, IMØDE, ITEST, IPLØT

Variable name	Description
NØSSP	No. of points in the sound speed profile. Each point corresponds to a depth $z$ at which the values of $c$ , $v$ , $\alpha$ , $\beta$ , $\rho$ and $\sigma$ are supplied. Values at both the source and the receiver depths <u>must</u> be included in the profile. See CARD 2.
IMØDE	Flag to select the method of computation.  IMØDE = 0 gives fast field method = 1 gives normal mode method
ITEST	Flag to select the internal test case profile. All default parameters for the test case correspond to those used in the AESD Workshop Case 1B. <sup>16</sup>  ITEST = 0 gives user-supplied profile = 1 gives internal profile
IPLØT	Flag to save the kernel and propagation loss values (fast field output) or excitation function and propagation loss values (normal mode output) in the file 17HH.PLT for subsequent access by the plotting program PLØT17HH.  IPLØT = 0 gives no plot file = 1 gives plot file

CARD 2 -- inputs ((V(I,J), J=1,7), I=1,NØSSP) -- FORMAT (7D10.0)

Variable Name	Description
V(I,J)	Array of physical properties of the environmental profile. The values at the source and receiver depths <u>must</u> be included in the profile. Each point in the profile separates layers having different acoustic properties. Discontinuities in acoustic properties can be accommodated by assigning two sets of values at the same depth. For each I-index profile point, the 7 physical values needed are
V(I,1)	z (m), Depth
V(I,2)	c (m/s), Pressure-wave sound speed
V(I,3)	v (m/s), Shear-wave sound speed
V(I,4)	$\alpha$ (dB/km), Pressure-wave attenuation
V(I,5)	$\beta$ (dB/km), Shear-wave attenuation
V(I,6)	$\rho$ (g/cm <sup>3</sup> ), Density
V(I,7)	$\sigma$ (m), Rms roughness

Note: In the LDGO version of the code, the normal mode computational method was selected if  $V(I,4) = V(I,7) = 0$  for  $1 \leq I \leq NØSSP$ , and if REFLT0 = 0 (see CARD 5). In the NUSC version, if IMØDE = 0, and the profile attenuations and surface roughness are everywhere zero, then V(I,4) is set equal to  $\Delta k$  at all depths. ( $\Delta k$  is defined in RMIN in CARD 4.) This attenuation is subsequently removed from the solution.

CARD 3 -- NAMELIST &CARD3 inputs    ISRCE, IRCVR, IPRUN, NØFFT,  
    INEXT, ITAPR, IDISP, ICØNT

Variable Name	Description
ISRCE	Profile I-index of the source.
IRCVR	Profile I-index of the receiver.
IPRUN	Pruning factor to limit display of aliased propagation loss values. Only the first 1/IPRUN of the propagation loss versus range curve is displayed. This parameter applies to the fast field method only. IPRUN > 2.
NØFFT	No. of points of the sampled integrand to be used as input to the inverse FFT. This parameter applies to the fast field method only. NØFFT < 8192.
INEXT	Flag to select the entry point for the <u>next</u> data input sequence.  INEXT = 0 gives an exit after this case < 0 gives an entry point at CARD2 > 0 gives an entry point at CARD3
ITAPR	Flag to select the option of tapering the integrand before taking the inverse FFT.  ITAPR = 0 gives no tapering (square window) = 1 gives tapering at both ends
IDISP	Flag to select the field variable of interest for this data set.  IDISP = 0 gives pressure as output < 0 gives horizontal displacement > 0 gives vertical displacement
ICØNT	Flag to select the computational method for evaluating the branch line integral. This applies to the normal mode method only.  ICØNT = 0 gives discrete modes only < 0 gives fast field evaluation > 0 gives Gaussian quadrature evaluation

CARD 4 -- NAMELIST &CARD4 inputs   FREQ, SLVL, CMIN, CMAX,  
RMIN, RMAX, DELR

Variable Name	Description
FREQ	Source frequency (Hz)
SLVL	Source level (dB re 1 $\mu$ Pa @ 1 m)
CMIN	Sound speed minimum (m/s). $\omega$ /CMIN gives the highest wavenumber in the integration for the fast field method. For the normal mode method, it supplies the upper wavenumber limit for the root finding routine for the mode eigenvalues. If CMIN = 0, a default value will be determined from the sound speed profile for the normal mode method.
CMAX	Sound speed maximum (m/s). $\omega$ /CMAX gives the lowest wavenumber in the integration for the fast field method. For the normal mode method, it supplies the lower wavenumber limit for the root finding routine for the mode eigenvalues. If CMAX = 0, a default value will be determined from the sound speed profile for the normal mode method. In addition, the integration will start from zero for the fast field method.
RMIN	The starting range (in km) of the propagation loss curve for the normal mode method. For the fast field method, this range (in m) is given by $\Delta r = 2\pi / (N\emptyset FFT * \Delta k)$ where $(N\emptyset FFT - 1) \Delta k = (\omega / CMIN - \omega / CMAX).$
RMAX	The maximum range (in km) of the propagation loss curve for the normal mode method. For the fast field method, this range (in m) is given by $N\emptyset FFT * \Delta r$ .
DELR	The range step (in km) of the propagation loss curve for the normal mode method. For the fast field method, this step (in m) is given by $\Delta r = RMIN$ .

CARD 5 -- NAMELIST &CARD5 inputs REFLT0, ALPHAO, ATTENO, RHØ0, H

Variable Name	Description
REFLT0	Rms surface roughness (m) at $z = 0$ .  If REFLT0 $\neq 0$ , then the next three parameters are internally set to zero.
ALPHAO	Pressure-wave sound speed (m/s) of the <u>fluid</u> in the upper half-space $z < 0$ . This parameter determines whether this region is a vacuum or a fluid.
ATTENO	Pressure-wave attenuation (dB/km) of the <u>fluid</u> in the upper half-space $z < 0$ .
RHØ0	Density ( $\text{g/cm}^3$ ) of the <u>fluid</u> in the upper half-space $z < 0$ .
H	Separation distance (m) between the source and receiver when located within the <u>fluid</u> half-space $z < 0$ .  To use this option, the following requirements must be met:  <ol style="list-style-type: none"> <li>1. <math>V(1,2) = V(2,2) = 0</math>. See CARD2.</li> <li>2. <math>V(I+1,2) - V(I,2) \neq 0</math> for at least one value in the range <math>2 \leq I \leq NØSSP - 1</math>.</li> <li>3. <math>V(I,3) = 0</math> for <math>1 \leq I \leq NØSSP</math>.</li> <li>4. Both ALPHAO and H must be specified.</li> </ol>



## 3.2 DATA SEQUENCE FOR PLØT17HH

A plotting program (PLØT17HH) was developed to provide quality plots of the curves generated by NUSC17HH and stored in the output file named 17HH.PLT. Plotting is effected online so that prompts for data input are issued to a user's terminal. Plots can be directed to several display devices, including the Tektronix 4014, Calcomp 1039, and FR80. An explanation of the input prompts, which allow some flexibility in plotting the data, are given below.

Variable Name	Description
IBFIL	Flag to select plot device.  IBFIL = 2 to select Tektronix 4014 = 4 to select FR80 = 8 to select Calcomp 1039
ISPØT	Flag to select line thickness. This flag is used only for plots directed to the FR80.  ISPØT = 0-7 where the line thickness increases with ISPØT
IMØDE	Flag to identify the method of computation used in NUSC17HH.  IMØDE = 0 signifies the fast field method = 1 signifies the normal mode method
IUNIT	Flag to select the units of range and dB.  IUNIT = 0 gives km and dB re 1 m = 1 gives kyd and dB re 1 yd
RMIN	Minimum range displayed on the range axis.
RMAX	Maximum range displayed on the range axis.
RPIN	No. of range units per division on the range axis.
TMIN	Minimum dB level on the propagation loss axis.
TMAX	Maximum dB level on the propagation loss axis.
TPIN	No. of dB per division on the propagation loss axis.

## 4. COMMAND FILE SEQUENCE

The sample command file, designated NUSC17HH.COM, can be used to place the program NUSC17HH into the batch queue. The command file comprises the following lines:

\$ASSIGN NL SYS\$PRINT	line 1
\$ASSIGN 17HH.DAT FØR005	line 2
\$ASSIGN 17HH.PLT FØR007	line 3
\$RUN DBAO:[THØMSØN]NUSC17HH	line 4
\$CØPY NUSC17HH.LØG 17HH.ØUT	line 5
\$EXIT	line 6

Line 1 - Assigns the log file to the user's disc area.

Line 2 - Assigns the data file 17HH.DAT to unit 5.

Line 3 - Assigns the plot file 17HH.PLT to unit 7  
for subsequent access by the program PLØT17HH.

Line 4 - Runs the executable version of the program,  
i.e., NUSC17HH.EXE.

Line 5 - Copies the log file which contains all printed  
output from NUSC17HH (written to unit 6)  
to the output file 17HH.ØUT

Line 6 - Terminates the command file.

The command file is invoked by keying in "SUBMIT NUSC17HH". The plotting program PLØT17HH is invoked by keying in "RUN DBAO:[THØMSØN]PLØT17HH" and responding to the prompts described in section 3.2.

## 5. NUMERICAL EXAMPLES

In this section, we present several numerical examples to illustrate the computational capabilities of NUSC17HH and the graphical capabilities of PLØT17HH. The printed output of the model, which is stored in the file 17HH.ØUT, will not be described. However, since some of the printed output relates to the variable names used by the LDG0 version of the model, the user may find it convenient to refer to the equivalence list given in the appendix.

## 5.1 TEST CASE 1.

The first example (test case 1) is taken from an AESD Workshop on acoustic modeling.<sup>16</sup> The data input sequence for this example is shown in figure 4. By setting the flag ITEST = 1, all the parameters listed in figure 4 are set automatically via DATA statements, so that an equivalent data input sequence is given by (note that each "&" appears in column 2)

1	2	3	4	5	6	7
12345678901234567890123456789012345678901234567890123456789012345678						
&CARD1						
ITEST=1,						
&END						
&CARD3						
&END						
&CARD4						
&END						
&CARD5						
&END						

The canonical North Pacific Ocean sound speed profile for this case is depicted in figure 5. The ocean bottom comprises a uniform half-space of density  $1.9176 \text{ g/cm}^3$  and a sound speed of  $1555.52 \text{ m/s}$ . Calculations of the acoustic field were carried out at  $25 \text{ Hz}$  for a source at a depth of  $253.9 \text{ m}$  and a receiver depth of  $863.5 \text{ m}$ .

Figure 6 presents the results for test case 1 using the normal mode computational option. The discrete spectrum comprised 44 propagating modes. The contribution of the continuous spectrum was not included by setting ICØNT = 0 and limiting the search area of the root finding routine to the range of wavenumbers within  $\omega/\text{CMIN} = \omega/1471.88 < k < \omega/1555.52 = \omega/\text{CMAX}$  determined by the maximum and minimum values of the sound speed in the profile. Figure 6(a) shows the normalized magnitude of the excitation function of each mode in the sum. Figure 6(b) shows the propagation loss versus range curve, a coherent sum of 44 modes, which exhibits a well defined convergence zone behaviour for this example.

Figure 7 shows the results obtained for test case 1 using the fast field computational option. For these results, 512 points were used to sample the discrete mode region of the wavenumber axis. Figure 7(a) shows the normalized magnitude of the kernel of the integrand (the depth-dependent Green's function D) of equation (17). There is a direct correspondence between the peaks of the kernel in this figure and the locations of the excitation functions given

1 2 3 4 5 6 7  
12345678901234567890123456789012345678901234567890123456789012345678

&amp;CARD1

NØSSP=8,  
IMØDE=1,  
ITEST=0,  
IPLØT=1,

&amp;END

0.00	1536.50	0.00	0.00	0.00	1.00	0.00
152.40	1539.24	0.00	0.00	0.00	1.00	0.00
253.90	1524.01	0.00	0.00	0.00	1.00	0.00
406.30	1501.14	0.00	0.00	0.00	1.00	0.00
863.50	1479.19	0.00	0.00	0.00	1.00	0.00
1015.90	1471.88	0.00	0.00	0.00	1.00	0.00
5587.90	1549.60	0.00	0.00	0.00	1.00	0.00
5587.90	1555.52	0.00	0.00	0.00	1.9176	0.00

&amp;CARD3

ISRCE=3,  
IRCVR=5,  
IPRUN=2,  
NØFFT=512,  
INEXT=0,  
ITAPR=0,  
IDISP=0,  
ICØNT=0,

&amp;END

&amp;CARD4

FREQ=25.,  
SLVL=1.,  
CMIN=1471.88,  
CMAX=1555.52,  
RMIN=0.25,  
RMAX=200.,  
DELR=0.25,

&amp;END

&amp;CARD5

REFLTO=0.,  
ALPHA0=0.,  
ATTENO=0.,  
RHØ0=0.,  
H=0.,

&amp;END

Figure 4. Data Input Sequence for Test Case 1

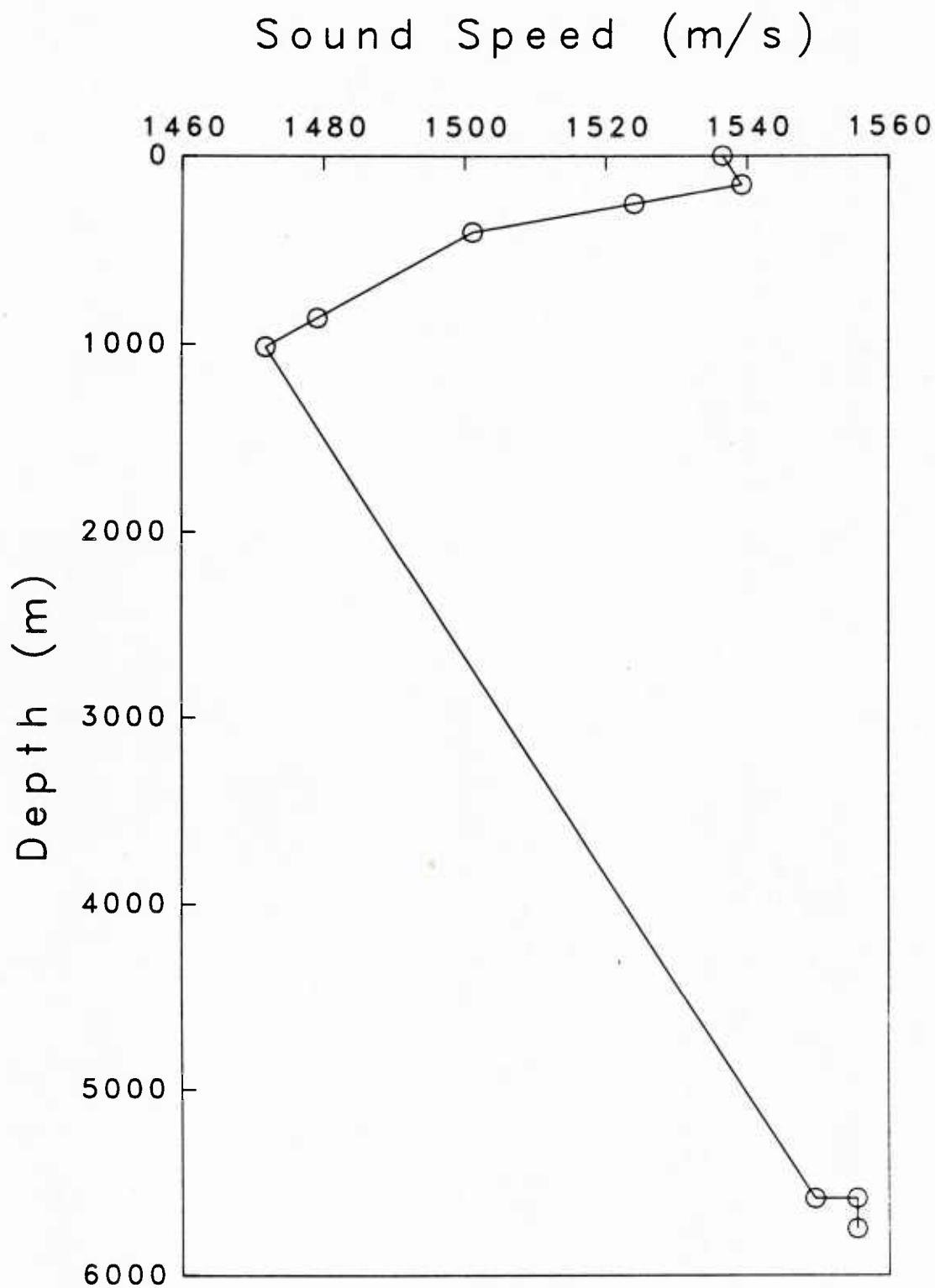


Figure 5. Sound Speed Profile for Test Case 1 (Source Depth = 253.9 m, Receiver Depth = 863.5 m,  $c_{N+1} = 1555.52$  m/s,  $\rho_{N+1} = 1.9176$  g/cm<sup>3</sup>)

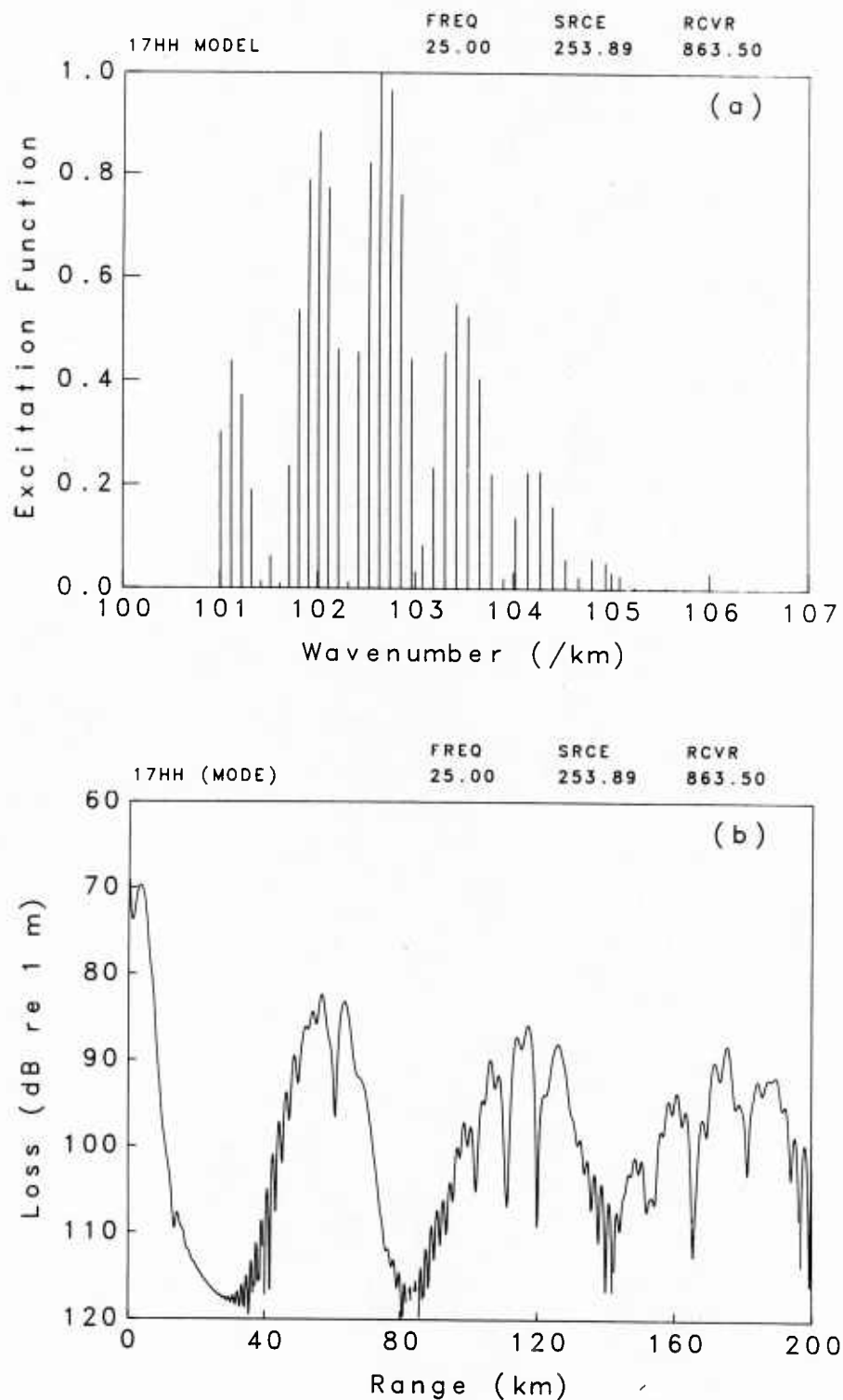


Figure 6. (a) Mode Excitation Functions Versus Wavenumber, and  
 (b) Associated Propagation Losses Versus Range  
 Test Case 1, Discrete Spectrum, Frequency = 25 Hz

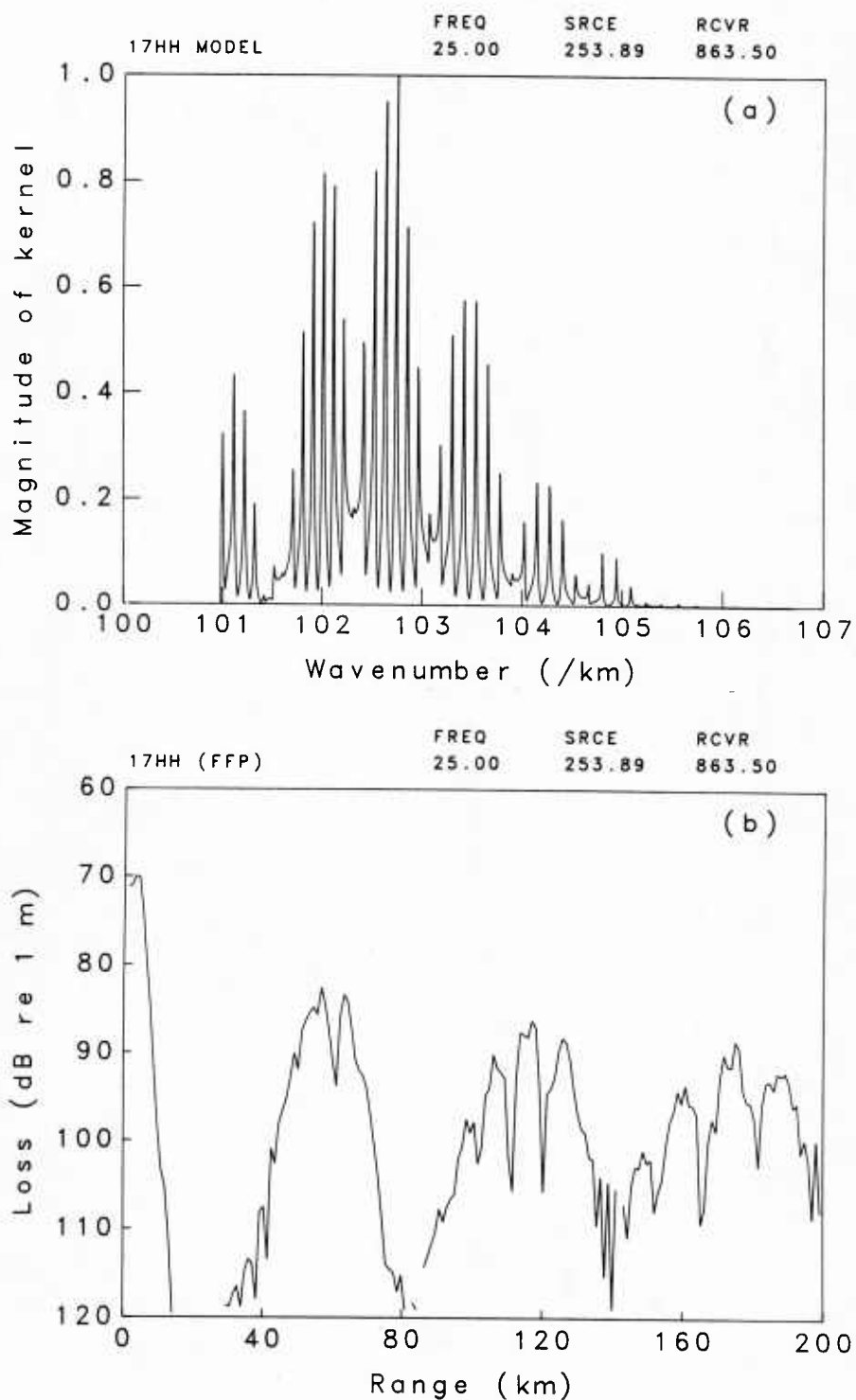


Figure 7. (a) Green's Function Kernel Versus Wavenumber, and  
(b) Associated Propagation Losses Versus Range  
Test Case 1, Discrete Spectrum, Frequency = 25 Hz



in Figure 6. This plot of the magnitude of the kernel function, however, includes the effect of the attenuation required to displace the poles from the real integration axis. As expected, after removing the effects of the added attenuation, the propagation loss versus range curve (figure 7(b)) for the fast field result agrees almost exactly with the corresponding curve determined by the normal mode method.

The contribution of the discrete spectrum gives rise to those propagating modes whose equivalent angles at the ocean bottom are less than that of the critical ray, i.e., those rays near grazing which reflect from the ocean floor without any loss into the bottom. This accounts for the high losses observed before the first convergence zone, a region that becomes "filled in" when the steeper angle bottom bounce rays (the continuous spectrum) are included in the calculations. This contribution is accommodated in the fast field method by sampling smaller wavenumbers. Figures 8 and 9 show the effects of increasing the value of CMAX to include these wavenumbers. In each case,  $\Delta k$  was fixed at the value used in figure 7 and figure 8(a) to span the discrete spectrum with  $N_{\text{FFT}} = 512$  points. In figure 8(b) the range of wavenumbers has been doubled as  $N_{\text{FFT}}$  is increased to 1024 points. Figure 9 shows the effects of further doubling of the wavenumber range using values of  $N_{\text{FFT}}$  of 2048 (figure 9(a)) and 4096 (figure 9(b)) points. This sequence of results shows the effects of increasing steeper angle equivalent rays as the range of the wavenumbers included in the integration is increased. Since these rays correspond to the bottom bounce contributions, the region before the first convergence zone is steadily filled in. While it is evident that the contribution of the bottom bounce energy is now included in the computation, the structure of the convergence zones are not affected by these higher angle ray arrivals. (The equivalent ray angles at the source for each of the CMAX values used in the calculations is indicated.)

As a final computation for this profile, figure 10 shows the normal mode result when the frequency was increased to 250 Hz. In this case, 437 propagating modes were determined. The structure of the excitation functions versus wavenumber changes significantly from that shown in figure 5. The dominant group of modes now occurs near the highest wavenumbers. As a result, the propagation loss versus range curve (figure 10(b)) shows constructive interference near the leading part of each zone. NUSC17HH can identify up to 500 propagating modes. This example was included to indicate that apparently no computational difficulties arise in determining sound propagation for relatively high frequency, deep water conditions.

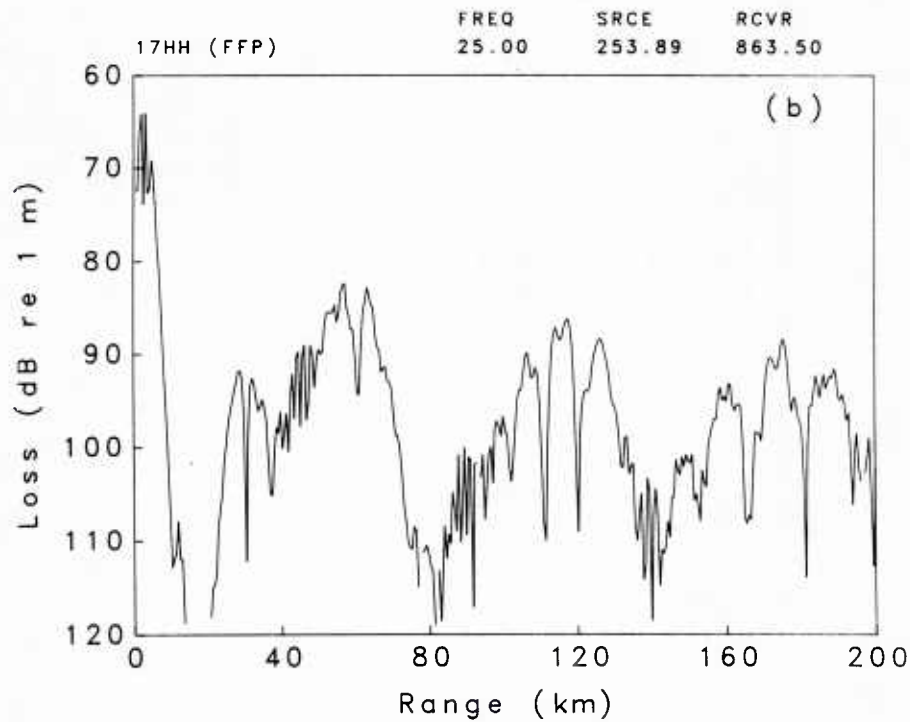
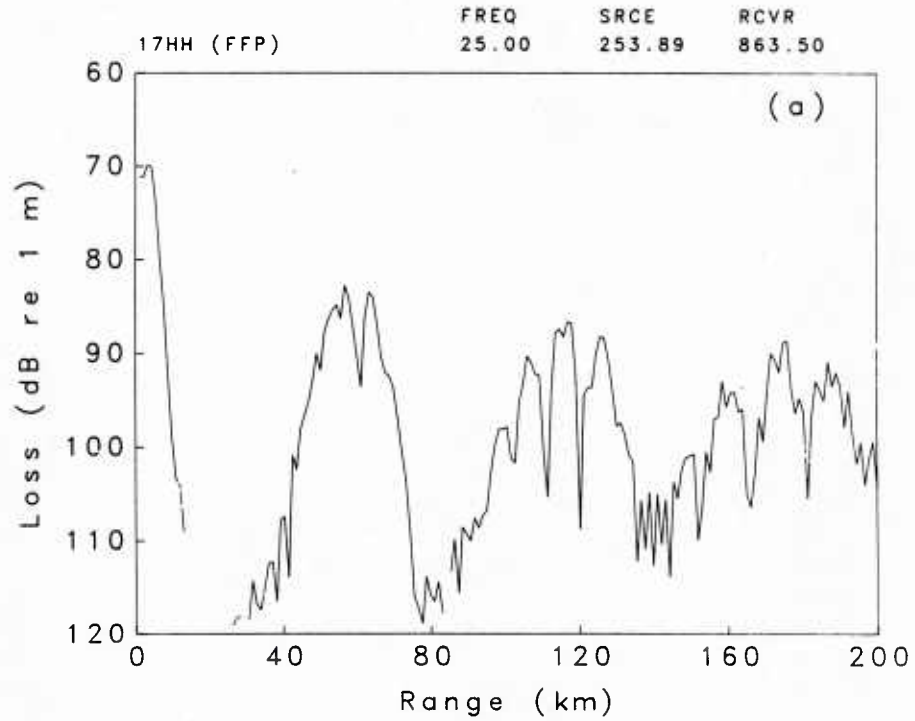


Figure 8. Fast Field Propagation Losses Versus Range, Test Case 1  
 Discrete Plus Continuous Spectrum, Frequency = 25 Hz  
 (a)  $N_{\text{FFT}} = 512$ ,  $C_{\text{MAX}} = 1555.52$  m/s, Source Aperture  $< 11.6^\circ$   
 (b)  $N_{\text{FFT}} = 1024$ ,  $C_{\text{MAX}} = 1649.43$  m/s, Source Aperture  $< 22.5^\circ$

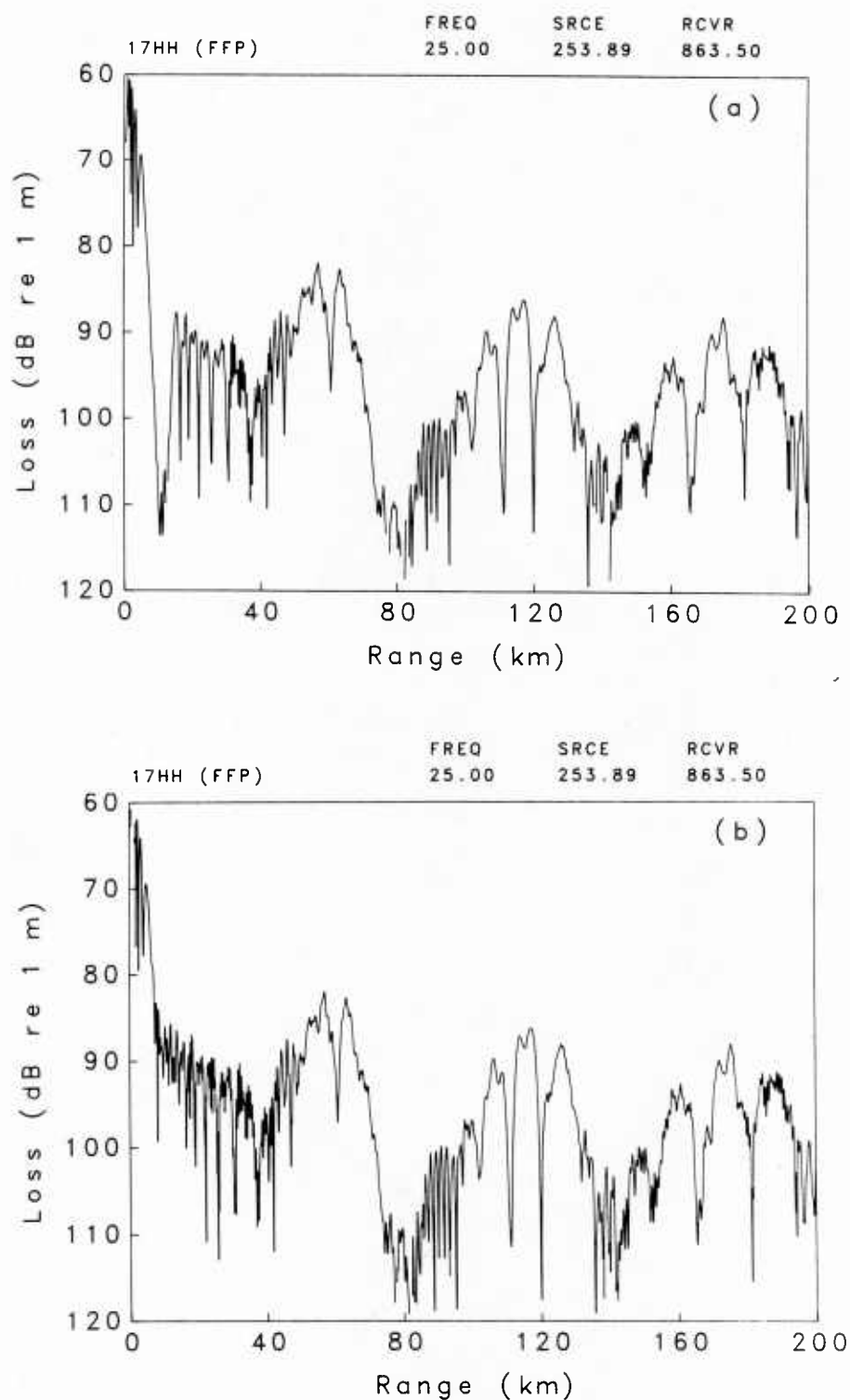


Figure 9. Fast Field Propagation Losses Versus Range, Test Case 1  
 Discrete Plus Continuous Spectrum, Frequency = 25 Hz  
 (a)  $N_{FFT} = 2048$ ,  $C_{MAX} = 1875.95$  m/s, Source Aperture  $< 35.7^\circ$   
 (b)  $N_{FFT} = 4096$ ,  $C_{MAX} = 2586.31$  m/s, Source Aperture  $< 53.9^\circ$

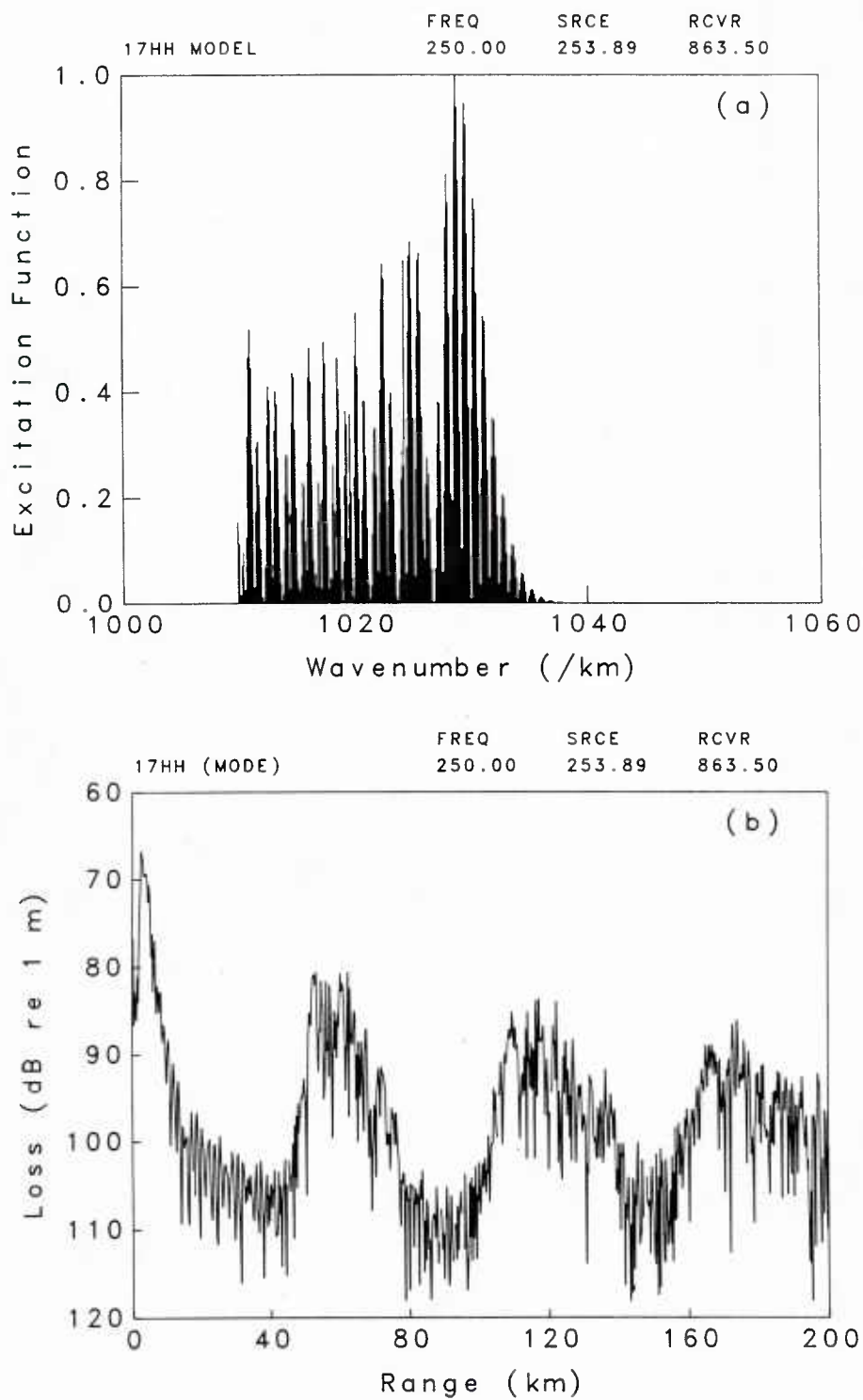


Figure 10. (a) Mode Excitation Functions Versus Wavenumber, and  
 (b) Associated Propagation Losses Versus Range  
 Test Case 1, Discrete Spectrum, Frequency = 250 Hz

## 5.2. TEST CASE 2

The data input sequence for the second test case is shown in figure 11 and the sound speed profile for this example is plotted in figure 12. This profile is representative of the Central Arctic Ocean and exhibits a pronounced surface duct. Since the entire profile is upward refracting, the bottom is modeled as a uniform half space of density  $1 \text{ g/cm}^3$  and sound speed equal to that at the base of the water column. For this example, calculations were made at a frequency of 50 Hz for a source depth of 91.44 m and a receiver depth of 137.14 m.

Using the fast field computational mode, the kernel versus wavenumber and associated propagation loss versus range plots are shown in figure 13. Only the region of the wavenumber axis spanned by the discrete modes was sampled with  $N_{\text{FFT}} = 2048$  points. The plot of the kernel indicates that the propagation is dominated by a single mode for these conditions. It is interesting to observe that the wavenumber for this mode does not correspond to an eigenray connecting the source and receiver, i.e., the turning point depth of the equivalent ray lies between the depths of the source and the receiver. Inspection of the propagation loss shows that the character of the curve is well described by cylindrical spreading. The convergence zone behaviour of the deep cycling rays is apparent at multiples of about 45 km. Figure 14 depicts the kernel and propagation loss when an rms surface roughness of 5 m is included in the calculations by setting the value of  $\text{REFLTO} = 5$ . The relative magnitude of the peaks in the kernel have changed from their values in figure 13 and the width of the dominant peak has increased. The effect on the propagation loss is to increase the loss from cylindrical spreading. This increase in loss can be determined from the two graphs to be approximately 0.06 dB/km.

The effect of adding a solid ice canopy to the sound speed profile is illustrated in figure 15. A 5 m thick ice sheet was inserted at the top of the profile with a density of  $0.9 \text{ g/cm}^3$ , a compressional sound speed of 3500 m/s, and a shear sound speed of 1800 m/s. We note that both  $\text{ISRCE}$  and  $\text{IRCVR}$  must be increased by 2 in order to maintain the previous source and receiver positions within the water profile. In addition, all profile depths were increased by 5 m. For this example, since the wavenumbers associated with the shear wave speed were not expected to contribute significantly for the source and receiver depths used in the calculations, only those wavenumbers spanning the maximum and minimum values of compressional sound speed in the water column were considered in the integration. As a result, the effects of the shear waves entered only through the boundary conditions satisfied at layer interfaces.

Comparing figures 13 and 15, it is evident that the presence of the ice layer increases the propagation loss by only a few dB. On the other hand, the structure of the propagation loss curve in figure 15 is altered considerably from that shown in figure 13. Comparison of the two kernels indicates that the ice layer redistributes the energy between the lowest three modes. The effect on the propagation loss curve is to enhance the interference pattern between the second and third modes giving rise to a beating appearance superimposed on the cylindrical spreading loss associated with the dominant first mode.

TR 7221

	1		2		3		4		5		6		7	
12345678901234567890123456789012345678901234567890123456789012345678														

&CARD1

NØSSP=16,  
IMØDE=0,  
ITEST=0,  
IPLØT=1,

&END

0.00	1436.81	0.00	0.00	0.00	1.00	0.00
61.07	1438.71	0.00	0.00	0.00	1.00	0.00
91.44	1440.21	0.00	0.00	0.00	1.00	0.00
101.21	1440.69	0.00	0.00	0.00	1.00	0.00
137.14	1447.28	0.00	0.00	0.00	1.00	0.00
190.67	1457.07	0.00	0.00	0.00	1.00	0.00
240.36	1459.71	0.00	0.00	0.00	1.00	0.00
352.99	1461.39	0.00	0.00	0.00	1.00	0.00
422.02	1461.62	0.00	0.00	0.00	1.00	0.00
498.50	1462.60	0.00	0.00	0.00	1.00	0.00
622.77	1462.85	0.00	0.00	0.00	1.00	0.00
924.17	1464.35	0.00	0.00	0.00	1.00	0.00
1266.52	1467.76	0.00	0.00	0.00	1.00	0.00
1939.09	1477.90	0.00	0.00	0.00	1.00	0.00
3657.60	1507.14	0.00	0.00	0.00	1.00	0.00
3657.60	1507.14	0.00	0.00	0.00	1.00	0.00

&CARD3

ISRCE=3,  
IRCVR=5,  
IPRUN=2,  
NØFFT=2048,  
INEXT=0,  
ITAPR=0,  
IDISP=0,  
ICØNT=0,

&END

&CARD4

FREQ=50.,  
SLVL=1.,  
CMIN=1436.81,  
CMAX=1507.14,  
RMIN=0.25,  
RMAX=200.,  
DELR=0.25,

&END

&CARD5

REFLT0=0.,  
ALPHA0=0.,  
ATTEN0=0.,  
RHØ0=0.,  
H=0.,

&END

Figure 11. Data Input Sequence for Test Case 2.

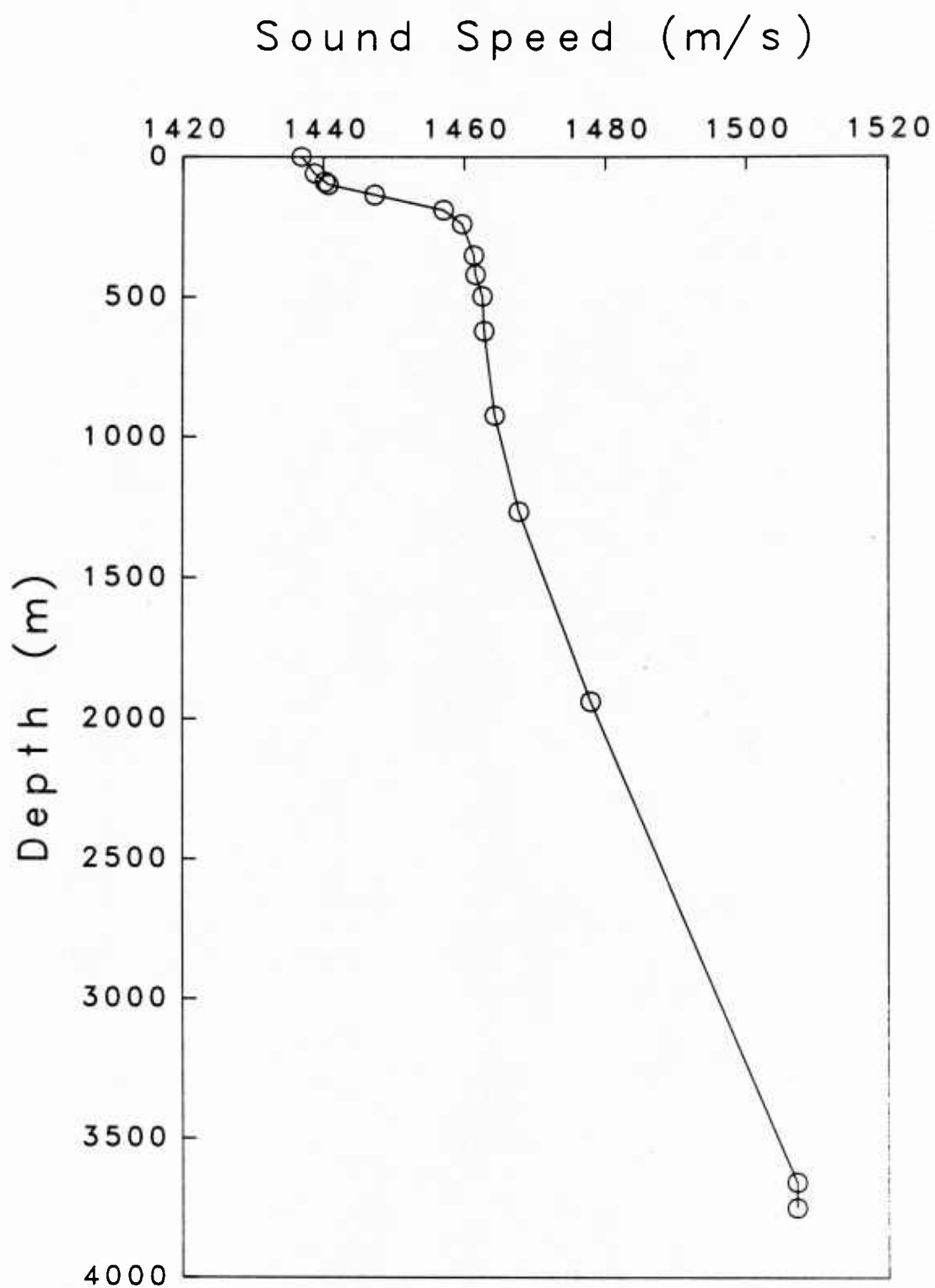


Figure 12. Sound Speed Profile for Test Case 2 (Source Depth = 91.44 m, Receiver Depth = 137.14 m,  $c_{N+1} = 1507.14$  m/s,  $\rho_{N+1} = 1.0$  g/cm<sup>3</sup>)



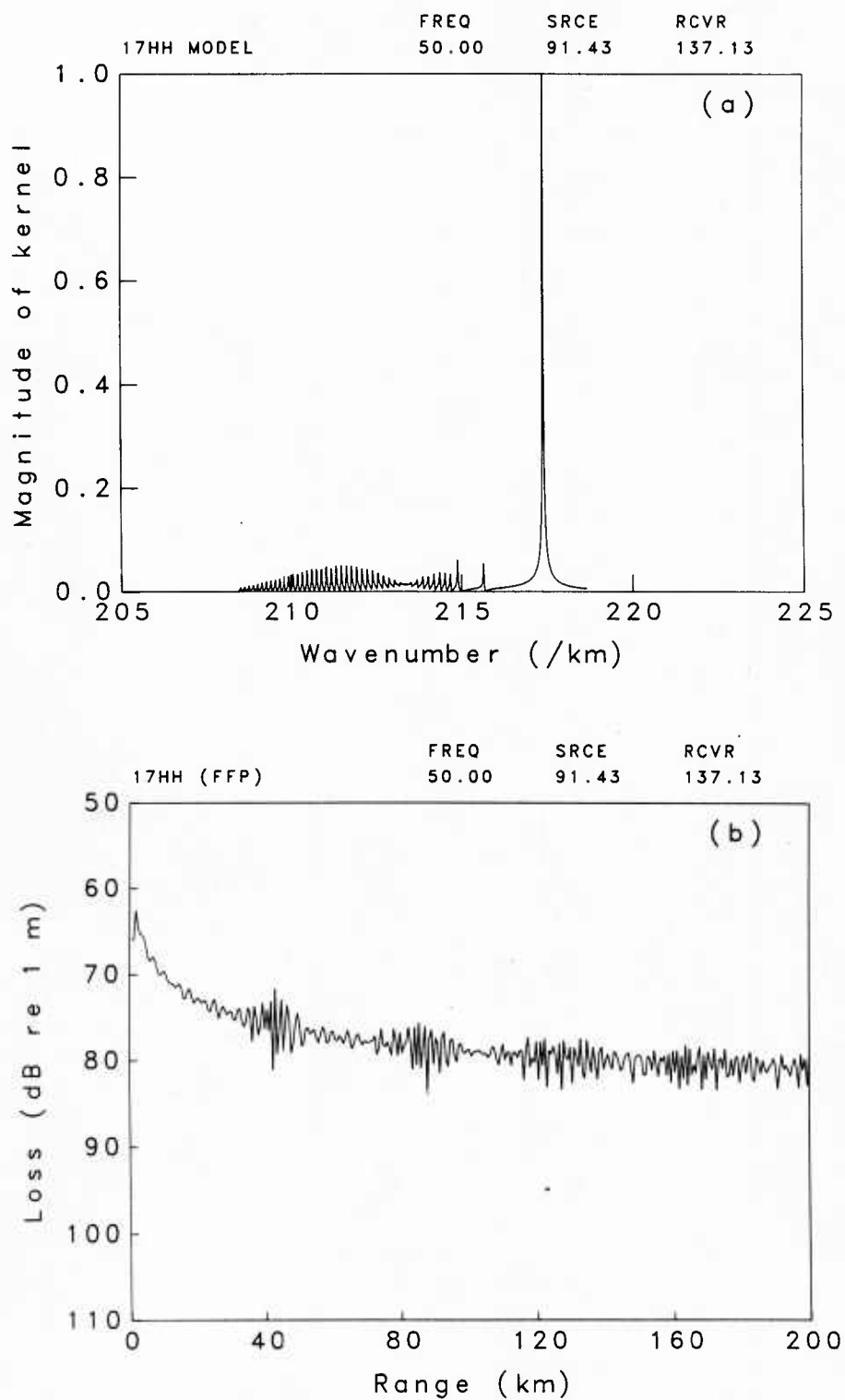


Figure 13. (a) Green's Function Kernel versus Wavenumber, and  
 (b) Associated Propagation Losses versus Range  
 Test Case 2, Discrete Spectrum, Frequency = 50 Hz,  $\sigma = 0$  m

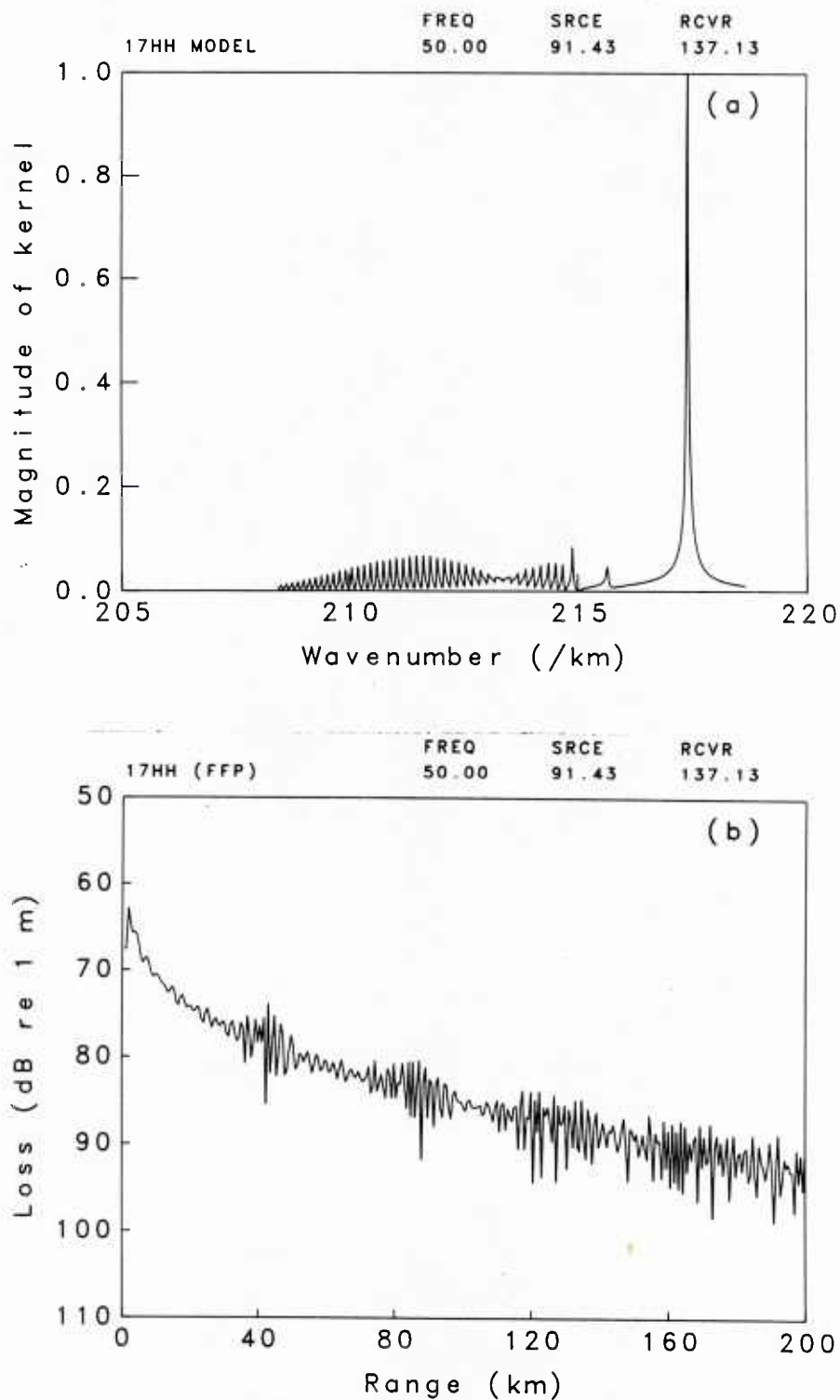


Figure 14. (a) Green's Function Kernel versus Wavenumber, and  
 (b) Associated Propagation Losses versus Range  
 Test Case 2, Discrete Spectrum, Frequency = 50 Hz,  $\sigma = 5$  m

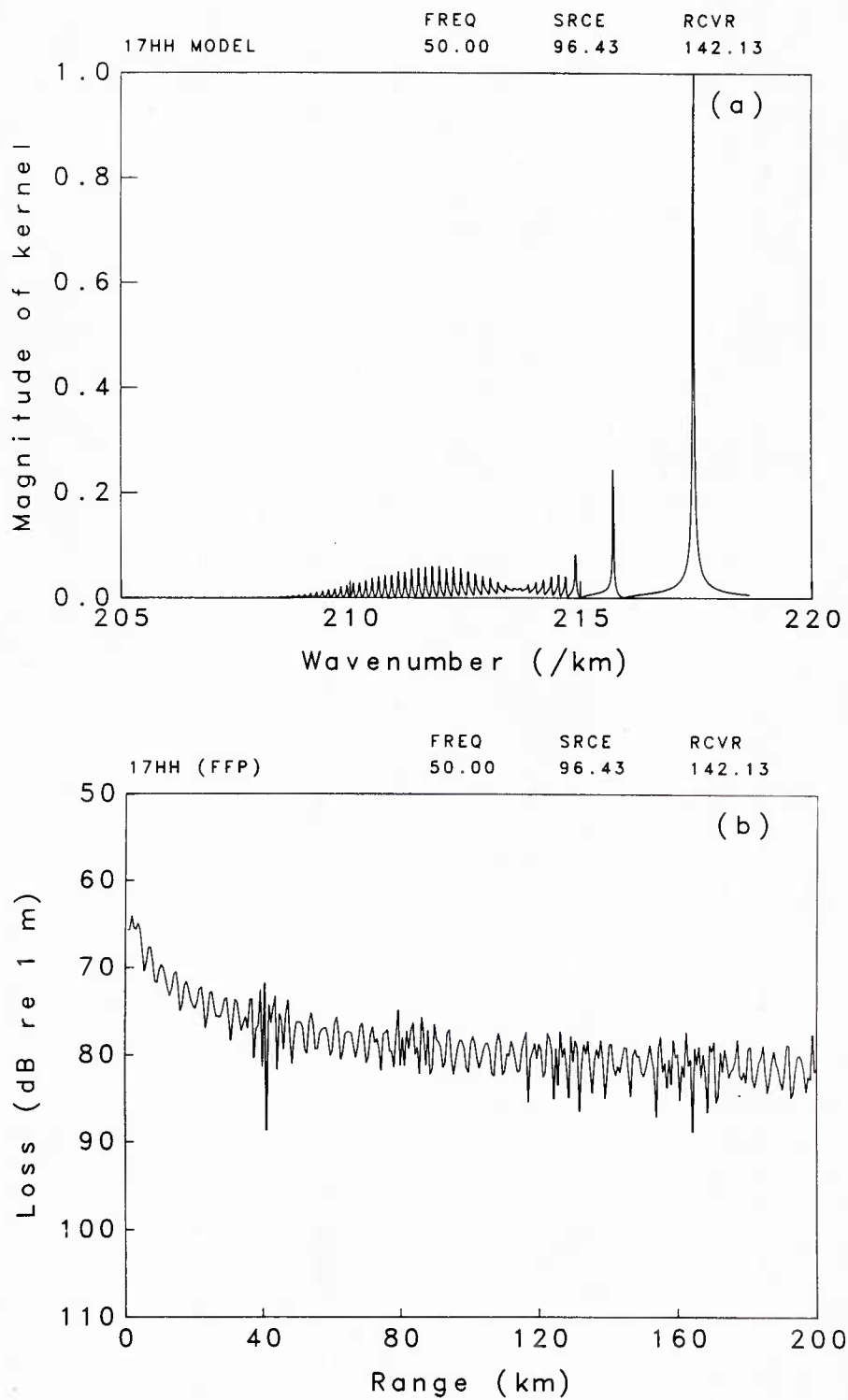


Figure 15. (a) Green's Function Kernel versus Wavenumber, and  
 (b) Associated Propagation Losses versus Range  
 Test Case 2, Discrete Spectrum, Frequency = 50 Hz, 5 m Ice Canopy

### 5.3. TEST CASE 3

The data input sequence for test case 3 is given in figure 16. For this shallow water profile, shown in figure 17, the bottom is expected to play an important role in the propagation of underwater sound. Moreover, the effects of the continuous spectrum will be seen to be important. Calculations were carried out for a frequency of 100 Hz, a source depth of 30 m, and a receiver depth of 90 m.

Figure 18 shows the discrete mode results for this test case. Only three proper modes were able to propagate under these conditions. The coherent sum of the three modes (figure 18(a)) determines the propagation loss versus range curve shown in the bottom part of the figure. With only three modes propagating, the character of the propagation loss versus range curve (figure 18(b)) is seen to be smooth. Figure 19 shows the results when the fast field computational option is used and part of the continuous spectrum is included in the integration ( $C_{MAX} = 1600$  m/s). It is apparent from the plot of the kernel (figure 19(a)) that in addition to the three peaks at the locations of the wavenumbers of the discrete modes, a considerable contribution arises in the adjacent span of the continuous spectrum. The effect on the propagation loss curve (figure 19(b)) is to modulate the discrete mode result of the previous figure.

According to the flowchart of figure 3, an alternate option of obtaining the fast field result is to evaluate numerically the branch line integral associated with the modal representation. Figure 20 presents the result of this computation when the branch line integral is evaluated via the fast field method by setting the flag  $ICONT < 0$ .  $N_{FFT}$  was set to 4096 points to ensure that the span of the unaliased range values reached 20 km. For comparison, another fast field computation is shown in figure 20(a) where  $C_{MAX}$  was increased to 1800 m/s and  $N_{FFT}$  was increased to 2048 points. While the propagation loss versus range curves are similar for the two methods of computation, the differences can be attributed to the points raised in the discussion in section 3.5. In particular, the branch line integral only included the portion around the real axis and the sound speed profile of the water column was taken to consist of isovelocity layers for the branch line evaluation. It is apparent that the fast field method of calculation gives the correct result with much less effort in this case. Efforts to compute the branch line contribution via numerical integration using Gaussian quadrature techniques did not prove successful.

TR 7221

1 2 3 4 5 6 7  
12345678901234567890123456789012345678901234567890123456789012345678

&CARD1

NØSSP=6,  
IMØDE=1,  
ITEST=0,  
IPLØT=1,

&END

0.00	1500.00	0.00	0.00	0.00	1.00	0.00
30.00	1499.50	0.00	0.00	0.00	1.00	0.00
90.00	1498.50	0.00	0.00	0.00	1.00	0.00
120.00	1498.00	0.00	0.00	0.00	1.00	0.00
240.00	1500.00	0.00	0.00	0.00	1.00	0.00
240.00	1505.00	0.00	0.00	0.00	2.10	0.00

&CARD3

ISRCE=2,  
IRCVR=3,  
IPRUN=2,  
NØFFT=1024,  
INEXT=0,  
ITAPR=0,  
IDISP=0,  
ICØNT=0,

&END

&CARD4

FREQ=100.,  
SLVL=1.,  
CMIN=1498.,  
CMAX=1505.,  
RMIN=0.1,  
RMAX=20.,  
DELR=0.1,

&END

&CARD5

REFLTO=0.,  
ALPHA0=0.,  
ATTENO=0.,  
RHØ0=0.,  
H=0.,

&END

Figure 16. Data Input Sequence for Test Case 3.

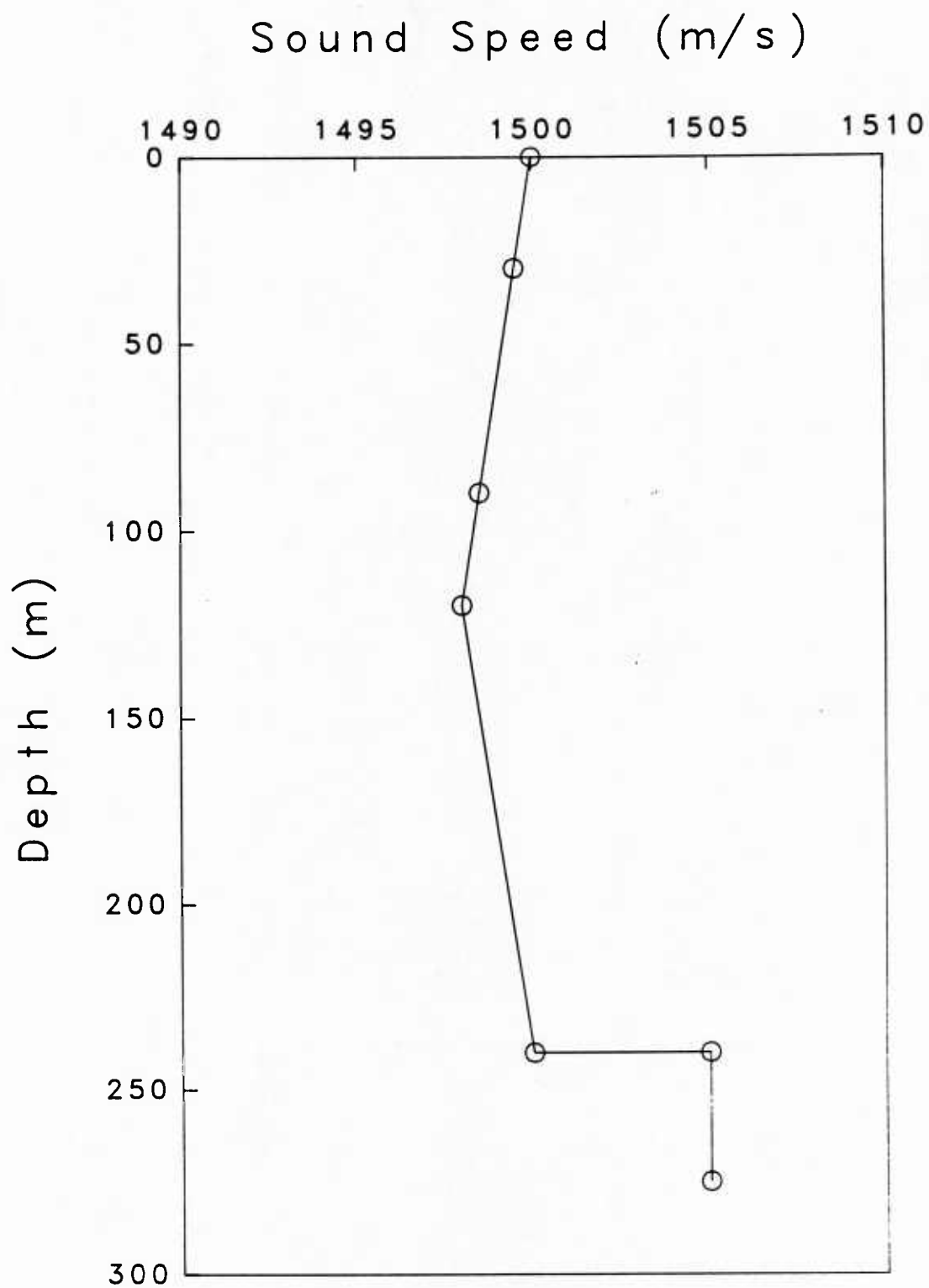


Figure 17. Sound Speed Profile for Test Case 3 (Source Depth = 30 m, Receiver Depth = 90 m,  $c_{N+1} = 1505$  m/s,  $\rho_{N+1} = 2.1$  g/cm<sup>3</sup>)

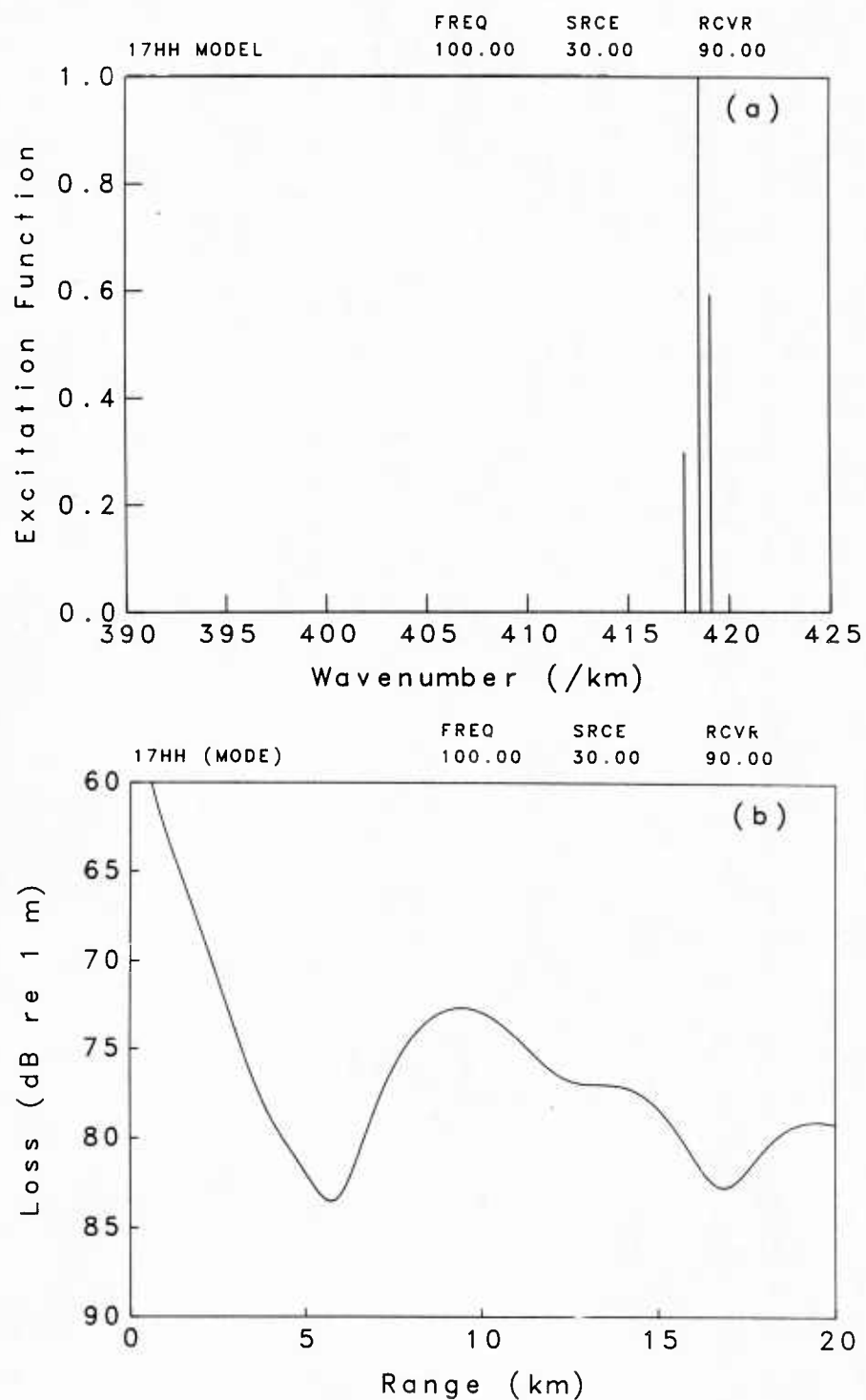


Figure 18. (a) Mode Excitation Functions versus Wavenumber, and  
(b) Associated Propagation Losses Versus Range  
Test Case 3, Discrete Spectrum, Frequency = 100 Hz

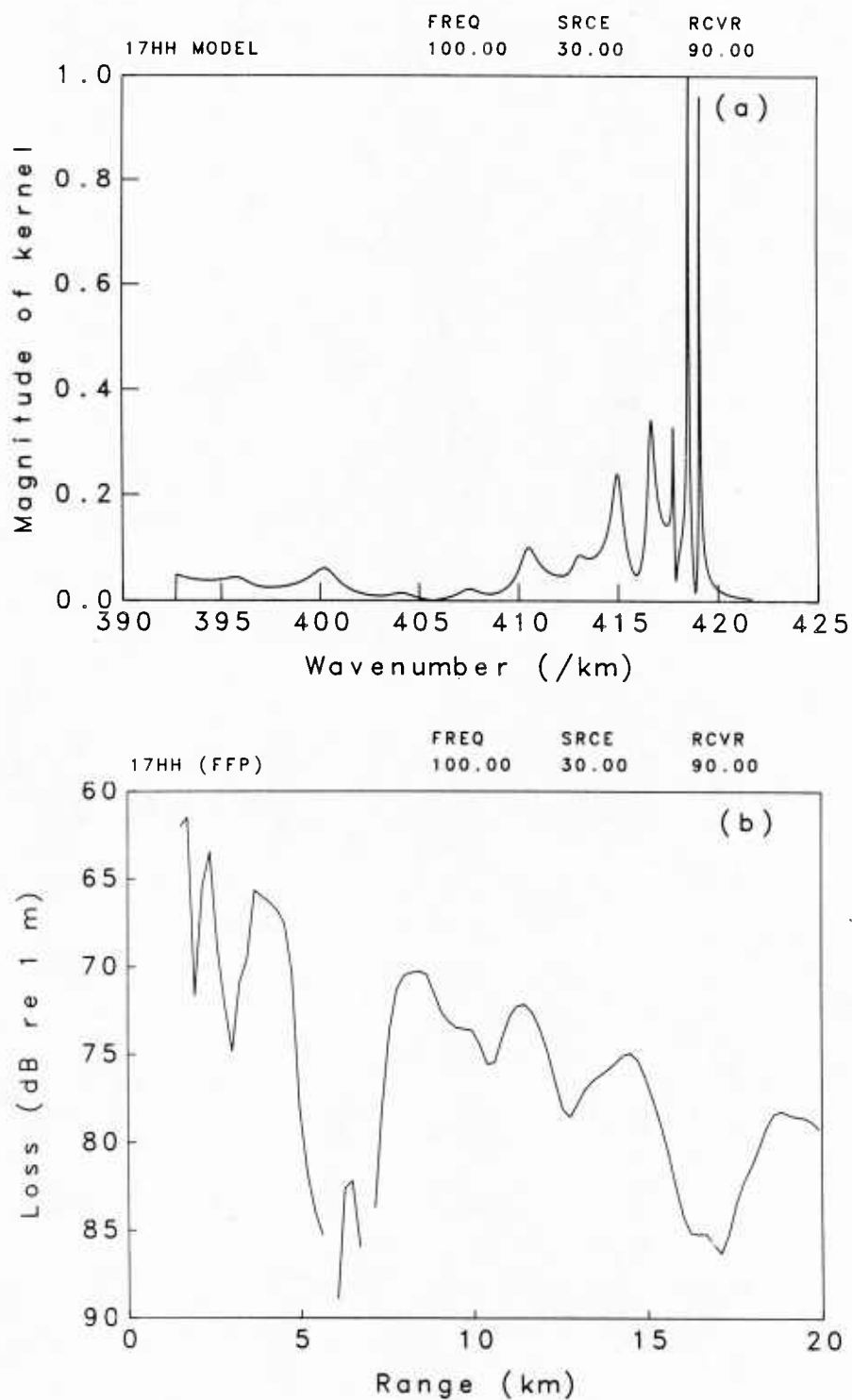


Figure 19. (a) Green's Function Kernel Versus Wavenumber, and  
 (b) Associated Propagation Losses Versus Range  
 Test Case 3,  $N_{\text{FFT}} = 1024$ ,  $C_{\text{MAX}} = 1650$  m/s, Frequency = 100 Hz



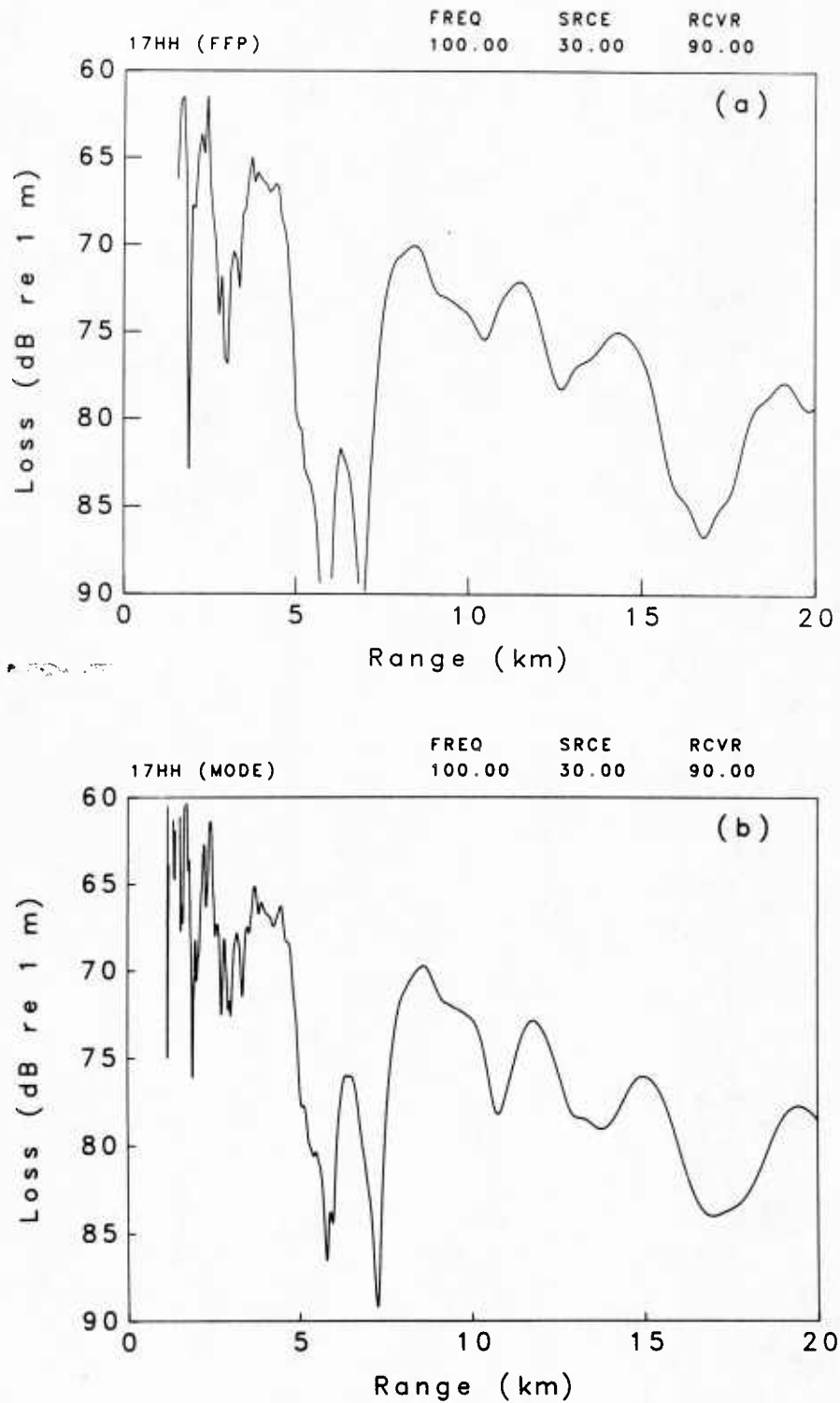


Figure 20. Propagation Losses versus Range, Test Case 3, Frequency = 100 Hz  
 (a) Fast Field Method,  $N_{\text{FFT}} = 2048$ ,  $C_{\text{MAX}} = 1800$  m/s  
 (b) Normal Mode Method,  $N_{\text{FFT}} = 4096$ ,  $IC_{\text{NT}} < 0$

#### 5.4. TEST CASE 4

This final example was taken from a recent workshop<sup>17</sup> and was included here to represent propagation in shallow water over a lossy bottom. An excellent account of all the test cases in the workshop has been carried out using another version of the fast field model.<sup>18</sup> The data input sequence for this example is given in figure 21. This example is essentially an extension of the so-called Pekeris model in which the absorption of the bottom is not zero. The sound speed profile in figure 22 shows an isovelocity water layer of sound speed 1500 m/s and density 1 g/cm<sup>3</sup> overlaying a lossy fluid halfspace of sound speed 1590 m/s, density 2.1 g/cm<sup>3</sup> and absorption 76.83 dB/km (0.5 dB/wavelength). The calculations were carried out for a frequency of 250 Hz.

Since there is attenuation in the bottom half-space for this example, the normal mode method of computation cannot be used. Figure 23 shows the results of a fast field evaluation with the source and receiver located in the middle of the water layer at a depth of 50 m. Figure 23(a) presents the magnitude of the kernel as a function of wavenumber in which 11 propagating modes can be identified. For this source and receiver depth, it is evident that the lower order modes (slowest phase velocities) dominate the propagation. The effect of attenuation is not readily apparent on the propagation loss versus range curve (figure 23(b)) since the lower order modes do not penetrate significantly into the bottom half-space. Only the range interval between 5 km and 10 km has been plotted. Within this range interval, only the propagating modes contribute to the acoustic field, thus only that region of the wavenumber axis was sampled in the integration.

The effect of locating the source and receiver near the bottom of the water layer at a depth of 99.5 m is shown in figure 24. The distribution of dominant modes has shifted to the higher mode numbers (figure 24(a)). As a result, the acoustic field within the water is influenced more by the properties of the lower half-space since the higher order modes penetrate further into the bottom. The large increase in propagation loss (figure 24(b)) observed near a range of 7 km is due to the presence of absorption in the bottom and its considerable effect on these more deeply penetrating higher order modes.

TR 7221

	1		2		3		4		5		6		7	
12345678901	2345678901	2345678901	2345678901	2345678901	2345678901	2345678901	2345678901	2345678901	2345678901	2345678901	2345678901	2345678901	2345678901	2345678901

&CARD1

NØSSP=4,  
IMØDE=0,  
ITEST=0,  
IPLØT=1,

&END

0.00	1500.00	0.00	0.00	0.00	1.00	0.00
50.00	1500.00	0.00	0.00	0.00	1.00	0.00
100.00	1500.00	0.00	0.00	0.00	1.00	0.00
100.00	1590.00	0.00	76.83	0.00	1.20	0.00

&CARD3

ISRCE=2,  
IRCVR=2,  
IPRUN=2,  
NØFFT=512,  
INEXT=0,  
ITAPR=0,  
IDISP=0,  
ICØNT=0,

&END

&CARD4

FREQ=250.,  
SLVL=1.,  
CMIN=1490.,  
CMAX=1600.,  
RMIN=0.1,  
RMAX=10.,  
DELR=0.1,

&END

&CARD5

REFLT0=0.,  
ALPHA0=0.,  
ATTEN0=0.,  
RHØ0=0.,  
H=0.,

&END

Figure 21. Data Input Sequence for Test Case 4.

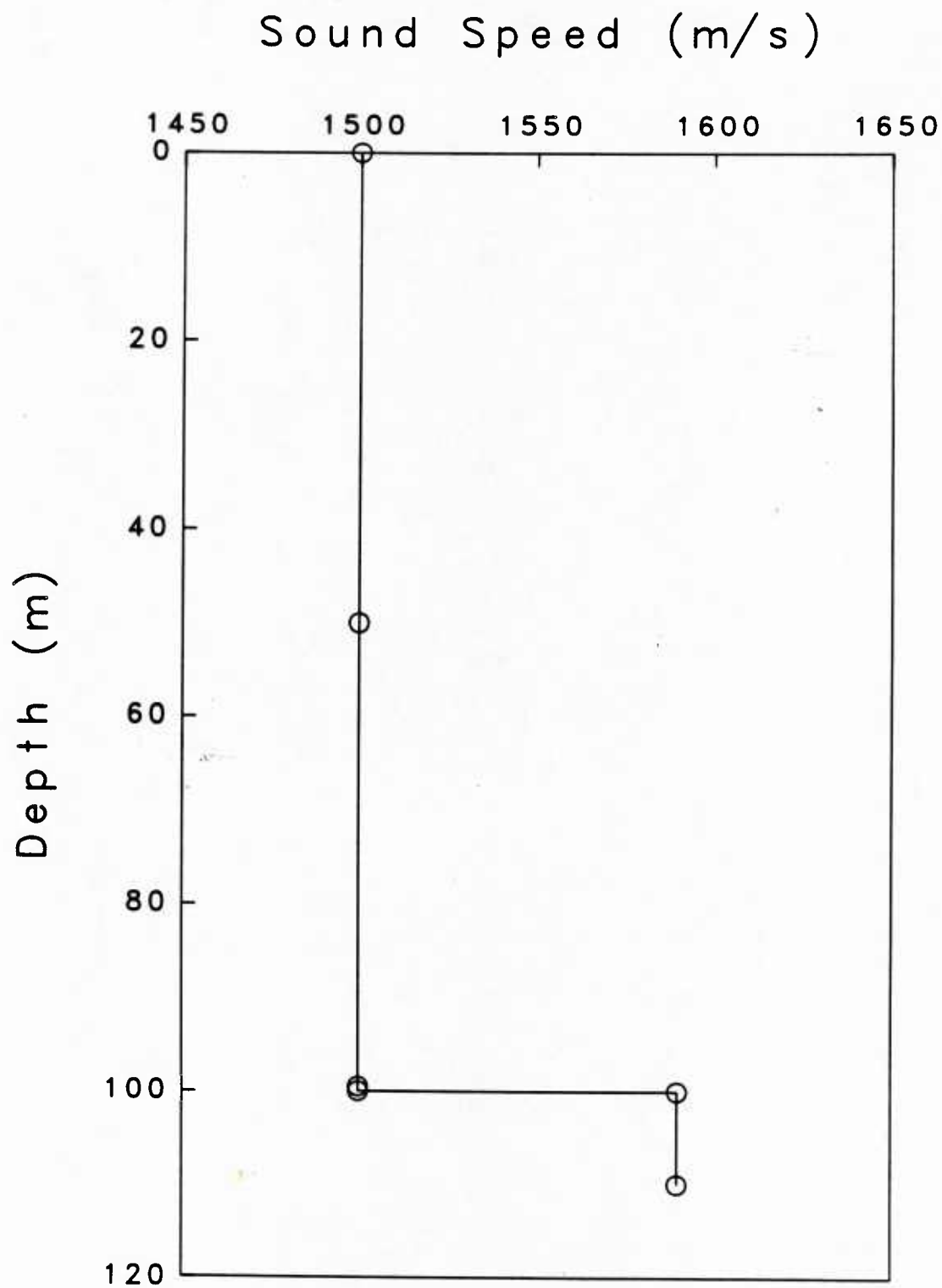


Figure 22. Sound Speed Profile for Test Case 4  
( $c_{N+1} = 1590$  m/s,  $\rho_{N+1} = 1.2$  g/cm<sup>3</sup>,  $\alpha_{N+1} = 76.83$  dB/km)

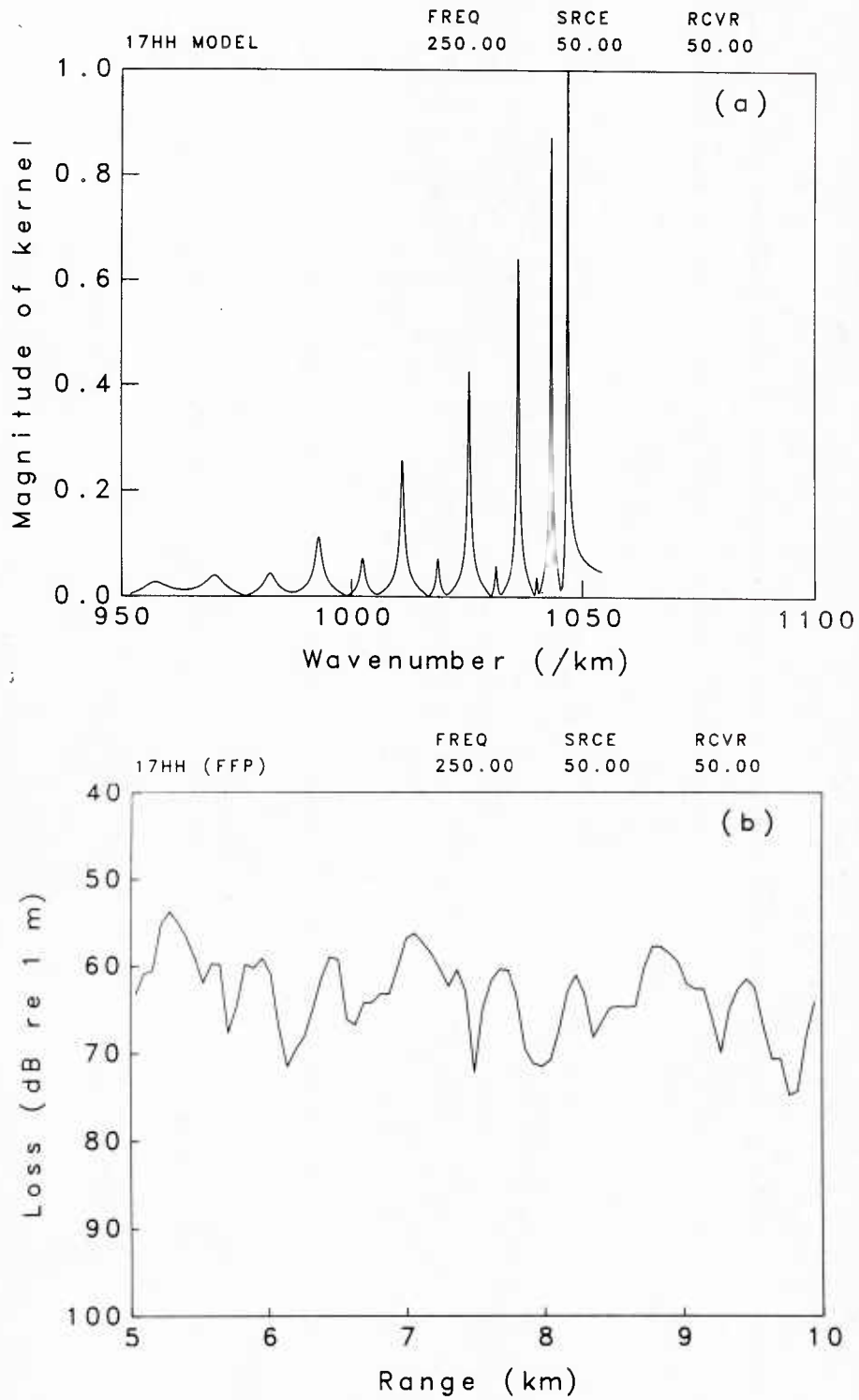


Figure 23. (a) Green's Function Kernel Versus Wavenumber, and (b) Associated Propagation Losses Versus Range, Test Case 4  
Source Depth = Receiver Depth = 50.0 m, Frequency = 250 Hz

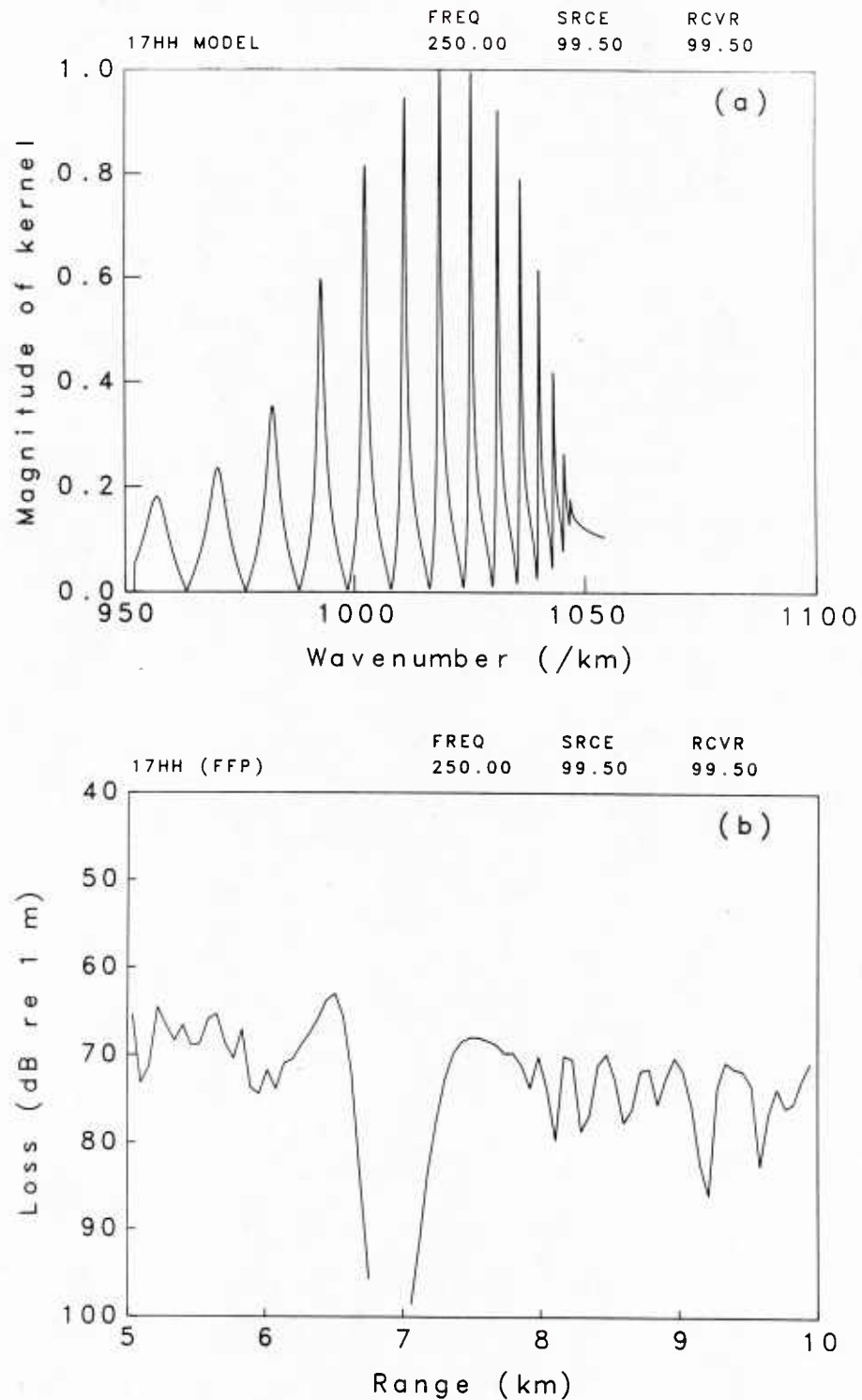


Figure 24. (a) Green's Function Kernel Versus Wavenumber, and (b) Associated Propagation Losses Versus Range, Test Case 4  
Source Depth = Receiver Depth = 99.5 m, Frequency = 250 Hz

## 6. SUMMARY

This report describes the implementation of the 17HH version of the LDGO normal mode/fast field model on the NUSC VAX 780/11 computer. This model differs from most propagation models used in underwater acoustics since it can treat both compressional and shear wave propagation within a layered fluid/solid medium. Sufficient documentation is provided to enable prospective NUSC users to obtain predictions of sound propagation. A plotting program is also described for obtaining quality graphs generated by the normal mode or fast field methods of computation. Several test cases have been provided (complete with data input sequences) to illustrate the use of the model under representative environmental conditions. Further examples of fast field method calculations may be found in a report by Jensen and Kuperman<sup>18</sup> in which several propagation loss models are compared.

The execution times for each of the test cases vary from a few seconds to more than an hour. Table 1 summarizes the actual CPU times required to obtain the information displayed in each Figure.

Table 1. CPU Execution Times for the Test Cases.

Test Case	Figure	CPU (minutes)
1	6	8.7
	7	3.5
	8(a)	3.5
	8(b)	8.1
	9(a)	16.5
	9(b)	31.5
	10	63.9
2	13	17.9
	14	17.1
	15	18.9
3	18	3.1
	19	5.5
	20(a)	10.1
	20(b)	12.5
4	23	0.5
	24	0.5

## 7. REFERENCES

1. F. R. DiNapoli and R. L. Deavenport, "Theoretical and Numerical Green's Function Field Solution in a Plane Multilayered Media," Journal of the Acoustical Society of America, vol. 67(1), 1980, pp. 92-105.
2. D. S. Ahluwalia and J. B. Keller, "Exact and Asymptotic Representations of the Sound Field in a Stratified Ocean," in Wave Propagation and Underwater Acoustics, ed. by J. B. Keller and J. S. Papadakis, Springer-Verlag, New York, 1977, pp. 14-84.
3. F. R. DiNapoli and R. L. Deavenport, "Numerical Models of Underwater Acoustic Propagation," in Ocean Acoustics, ed. J. A. DeSanto, Springer-Verlag, New York, 1978, pp. 79-157.
4. P. C. Etter, "Underwater Acoustic Modeling Techniques," Shock and Vibration Digest, vol. 13(2), 1981, pp. 11-20.
5. P. C. Etter, "Underwater Acoustic Modeling Techniques," Shock and Vibration Digest, vol. 16(1), 1984, pp. 17-23.
6. H. W. Kutschale, "The Integral Solution of the Sound Field in a Multilayered Liquid-Solid Half-Space with Numerical Computations for Low-Frequency Propagation in the Arctic Ocean," Lamont-Doherty Geological Observatory Technical Report No. 1, Palisades, New York, February 1970.
7. H. W. Kutschale, "Rapid Computation by Wave Theory of Propagation Loss in the Arctic Ocean," Lamont-Doherty Geological Observatory Technical Report No. 8, Palisades, New York, March 1973.
8. T. Akal and F. Jensen, "Effects of the Sea-Bed on Acoustic Propagation," in Acoustics and the Sea-Bed Conference Proceedings, ed. N. G. Pace, Bath University Press, Bath, 1983, pp. 225-232.
9. W. M. Ewing, W. S. Jardetzky, and F. Press, Elastic Waves in Layered Media, McGraw-Hill, New York, 1957, Ch. 4.
10. B. L. N. Kennett, Seismic Wave Propagation in Stratified Media, Cambridge University Press, Cambridge, 1983.
11. W. A. Kuperman, "Coherent Component of Specular Reflection and Transmission at a Randomly Rough Two-Fluid Interface," Journal of the Acoustical Society of America, vol. 58, 1975, pp. 365-370.
12. W. A. Kuperman and F. Ingenito, "Attenuation of the Coherent Component of Sound Propagating in Shallow Water with Rough Boundaries," Journal of the Acoustical Society of America, vol. 61(5), 1977, pp. 1178-1187.
13. R. L. Deavenport, "A Normal Mode Theory of an Underwater Acoustic Duct by Means of Green's Function," Radio Science, vol. 1(6), 1966, pp. 709-723.



14. H. P. Bucker, "Sound Propagation in a Channel with Lossy Boundaries," Journal of the Acoustical Society of America, vol. 48(5), 1970, pp. 1187-1194.
15. D. C. Stickler, "Normal-Mode Program with both the Discrete and Branch Line Contributions," Journal of the Acoustical Society of America, vol. 57(4), 1975, pp. 856-861.
16. C. W. Spofford, "A Synopsis of the AESD Workshop on Acoustic-Propagation Modeling by Non-Ray Tracing Techniques, 22-25 May 1973," AESD Technical Note 73-05, Arlington, VA, 1973.
17. J. A. Davis, D. White, and R. C. Cavanagh, "NORDA Parabolic Equation Workshop, 31 March - 3 April 1981," NORDA Technical Note 143, 1982.
18. F. B. Jensen and W. A. Kuperman, "Consistency Tests of Acoustic Propagation Models," SACLANTCEN Memorandum SM-157, 1 March 1982.

## APPENDIX

## EQUIVALENCE LIST BETWEEN LDGO AND NUSC DATA INPUT SEQUENCES

In the NUSC version of 17HH, the data input sequence has been modified from that supplied by LDGO. In addition to making use of the FORTRAN NAMELIST feature, most of the input variables have been renamed and their order of appearance within the data file has been changed. A comparison between the two input lists is given below. Upper case letters denote variable names which appear as indicated on each card image. Lower case letters identify equivalent variable names which appear on different card images. For example, KSF in the LDGO version has been renamed ISRCE in the NUSC version and both appear on the third card image. On the other hand, PO in the LDGO version has been renamed SLVL but has been relocated from the third card image to the fourth card image.

LDGO VERSIONNUSC VERSION

CARD 1 FØRMAT(2I3)

NAMELIST &amp;CARD1

MMAXF  
NCARD  
Not available  
Not available

NØSSP  
IPLØT  
IMØDE  
ITEST

CARD 2 ((V(I,J),J=1,7),I=1,MMAXF)  
FØRMAT(7D10.0)

CARD2 ((V(I,J),J=1,7),I=1,NØSSP)  
FØRMAT(7D10.0)

 $\alpha$  &  $\beta$  in Np/m $\alpha$  &  $\beta$  in dB/km

CARD 3 FØRMAT(7I5,4D10.0)

NAMELIST &amp;CARD3

KSF  
LRF  
MM  
LS  
KKK  
IBEAM  
IMAX  
FREQ  
PO  
C  
CMAX  
khpv see CARD4  
ibr see CARD4

ISRCE  
IRCVR  
IPRUN  
NØFFT  
INEXT  
ITAPR  
(rmax-rmin)/delr see &CARD4  
freq see &CARD4  
slvl see &CARD4  
cmin see &CARD4  
cmax see &CARD4  
IDISP  
ICØNT

LDGO version

## CARD 4 FORMAT(5D10.0,5I5)

REFLT0  
 ALPHA0  
 ATTEN0  
 RH00  
 H  
 INAUT  
 L0NG  
 KHPV  
 IBR  
 IDPL  
 freq       see CARD3  
 p0         see CARD3  
 c          see CARD3  
 cmax       see CARD3  
 ra         see CARD5  
 ra+imax\*dlra  
 dlra       see CARD5

## CARD 5 FORMAT(2D10.0)

RA  
 DLRA  
 reflt0     see CARD4  
 alpha0     see CARD4  
 atten0     see CARD4  
 rho0       see CARD4  
 h          see CARD4

NUSC version

## NAMELIST &amp;CARD4

reflt0       see &CARD5  
 alpha0       see &CARD5  
 atten0       see &CARD5  
 rho0         see &CARD5  
 h             see &CARD5  
 Set to 0 internally  
 Set to 1 internally  
 idisp         see &CARD3  
 icont         see &CARD3  
 Set to 1 internally  
 FREQ  
 SLVL  
 CMIN  
 CMAX  
 RMIN  
 RMAX  
 DELR

## NAMELIST &amp;CARD5

rmin           see &CARD4  
 delr           see &CARD4  
 REFLT0  
 ALPHA0  
 ATTEN0  
 RH00  
 H

## INITIAL DISTRIBUTION LIST

Addressee	No. of Copies
ASN (RE&S)	1
OUSDR&E (Research and Advanced Technology)	1
Principal Dep Assist Secretary (Research)	1
DARPA (TTO; Comdr. K. Evans)	2
CNO (OP-095; -098; -952D, Capt. E. Young, CDR H. Dantzler)	4
CNM (SPO PM-2; MAT-0723; -0724, Capt. E Harlett; -05, R. Hillyer; -907, L. L. Hill)	5
NAVELECSYSCOM (ELEX-12, R. Mitnick, J. Schuster; PME-124, R. Knudsen)	3
NAVSEASYSCOM (SEA-63; -63D; -63D3; -63R, D. Porter, F. Romano, R. Farwell; -63R-1; -63R-13)	8
NAVPGSCOL	1
DWTNSRDC	1
NORDA (Code 105; 320; 320, R. Lauer; 115, S. Marshall; 110A, R. Martin; 530, E. Chiaka, B. Blumenthal, W. Worsley, R. Wheatly; J. Matthews; G. Stanford; Library)	12
NOSC (712, M. Pederson, D. Gordon; 713, J. R. McCarthy; 7133, C. Persons; 1604, S. Sullivan; R. Smith; J. Lovett; G. Tunstall; Library)	9
NAVAIRDEVCEEN (J. Howard; B. Steinberg; P. Haas; Library)	4
NCSC	1
NAVSURFWPNCEN (R. Stevenson; M. Stripling; M. Stallard; Library)	4
NRL (5160, O. Diachok, R. Dicus; 5100, J. Munson; 5120, W. Mosley; 5109, A. Eller; Library)	6
MARINE PHYSICAL LAB, SCRIPPS (V. C. Anderson; F. Fischer; B. Williams)	3
NAVAIRSYSCOM (370B, E. David; 370J, W. Parrigian)	2
NISC (H. Foxwell)	1
ONR (ONR-102, R. Winokur; -102B; -200; -220, Capt. E. Craig, T. Warfield; -420, G. Hamilton; -422; -425AC; -4250A, J. McKisic; -425UA, P. Rogers; -100, J. A. Smith; -480)	12
DIA	1
CHESNAVFACENGCOM	1
ARL (University of Texas) (P. Vidmar; K. Hawker; R. Koch; Library)	4
ARL (Penn State University) (S. McDaniel; D. McCammon; Library)	3
Courant Institute (D. C. Stickler; Library)	2
Science Applications, Inc. (C. W. Spofford, R. Greene)	2
Cornell University (H. Schwetlick)	1
Northwestern University (G. Kriegsmann)	1
University of Denver (F. Hagin)	2
University of Miami (F. Tappert)	1
General Instrument Company (R. Breton)	1
FWG (P. Wille)	1
Woods Hole Oceanographic Institution (G. V. Frisk; Library)	2
Colorado School of Mines (J. A. DeSanto)	1
University of Victoria (J. T. Weaver; H. W. Dosso)	2
LDGO (H. W. Kutschale)	1
SACLANT (F. B. Jensen, H. Schmidt)	2

## INITIAL DISTRIBUTION LIST (Cont'd)

## DREP DISTRIBUTION

FMO

Victoria, BC, Canada VOS 180

## Addressee

No. of  
Copies

## CANADA

DREP 20  
 DSIS (Microfiche Section, Report Collection) 3  
 DREA 1  
 ORAE Library (DMOR) 2  
 CDLS/L CDR 1  
 CDLS/W CDR 1  
 CMDO 1  
 DMRS 1  
 Commander Maritime Command (MC/ORD, SSO Ocean) 2  
 CFMWS 1  
 Maritime Headquarters Pacific (SSO Op Rsch) 1  
 DST(SE)3 1  
 DTA(M)3 1  
 RRMC (Dept. of Oceanography) 1  
 D Met Oc 1  
 Project Officer IEP ABCANZ-2, NOP 981, Pentagon 3

## BRITAIN

DRIC 3  
 AUWE 1  
 RAE 1

## AUSTRALIA

DRC 1

## NEW ZEALAND

DSE 1

U216526

